TESS Hunt for Young and Maturing Exoplanets (THYME) III: a two-planet system in the 400 Myr Ursa Major Group

ANDREW W. MANN,[1] MARSHALL C. JOHNSON,[2] ANDREW VANDERBURG,[3, *] ADAM L. KRAUS,[3] AARON C. RIZZUTO,[3, †]
MACKENNA L. WOOD,[1] JONATHAN L. BUSH,[1] KEIGHLEY ROCKCLIFFE,[4] ELISABETH R. NEWTON,[4] DAVID W. LATHAM,[5]
ERIC E. MAMAJEK,[6] GEORGE ZHOU,[5, ‡] SAMUEL N. QUINN,[5] PA CHIA THAO,[1, §] SERENA BENATTI,[7] ROSARIO COSENTINO,[8]
SILVANO DESIDERA,[9] AVET HARUTYUNYAN,[8] CHRISTOPHE LOVIS,[10] ANNELIES MORTIER,[11] FRANCESCO A. PEPE,[10]
ENNIO PORETTI,[8, 12] THOMAS G. WILSON,[13] MARTTI H. KRISTIANSEN,[14, 15] ROBERT GAGLIANO,[16] THOMAS JACOBS,[17]
DARYLL M. LACOURSE,[18] MARK OMOHUNDRO,[19] HANS MARTIN SCHWENGELER,[20] IVAN A. TERENTEV,[21]
STEPHEN R. KANE,[22] MICHELLE L. HILL,[22] MARKUS RABUS,[2, 23] GILBERT A. ESQUERDO,[5] PERRY BERLIND,[5]
KAREN A. COLLINS,[5] GABRIEL MURAWSKI,[24, 25] MICHAEL M. AITKEN,[25] NEZAR HAZAM SALLAM,[25] BOB MASSEY,[26]
GEORGE R. RICKER,[27] ROLAND VANDERSPEK,[27] SARA SEAGER,[27, 28, 29] JOSHUA N. WINN,[30] JON M. JENKINS,[31]
THOMAS BARCLAY,[32, 33] DOUGLAS A. CALDWELL,[34, 31] DIANA DRAGOMIR,[35] JOHN P. DOTY,[36] ANA GLIDDEN,[28, 27]
PETER TENENBAUM,[34, 31] GUILLERMO TORRES,[5] JOSEPH D. TWICKEN,[34, 31] AND STEVEN VILLANUEVA JR[27, ¶]

[1]*Department of Physics and Astronomy, The University of North Carolina at Chapel Hill, Chapel Hill, NC 27599, USA*
[2]*Las Cumbres Observatory, 6740 Cortona Dr., Ste. 102, Goleta, CA 93117, USA*
[3]*Department of Astronomy, The University of Texas at Austin, Austin, TX 78712, USA*
[4]*Department of Physics and Astronomy, Dartmouth College, Hanover, NH 03755, USA*
[5]*Center for Astrophysics | Harvard & Smithsonian, 60 Garden Street, Cambridge, MA 02138, USA*
[6]*Jet Propulsion Laboratory, California Institute of Technology, 4800 Oak Grove Dr., Pasadena, CA 91109, USA*
[7]*INAF – Osservatorio Astronomico di Palermo, Piazza del Parlamento 1, I-90134, Palermo, Italy*
[8]*Fundación Galileo Galilei-INAF, Rambla José Ana Fernandez Pérez 7, 38712 Breña Baja, TF, Spain*
[9]*INAF – Osservatorio Astronomico di Padova, Vicolo dell'Osservatorio 5, I-35122, Padova, Italy*
[10]*Observatoire Astronomique de l'Université de Genève, 51 chemin des Maillettes, 1290 Versoix, Switzerland*
[11]*Astrophysics Group, Cavendish Laboratory, University of Cambridge, J.J. Thomson Avenue, Cambridge CB3 0HE, UK*
[12]*INAF-Osservatorio Astronomico di Brera, via E. Bianchi 46, 23807 Merate (LC), Italy*
[13]*School of Physics and Astronomy, University of St Andrews, North Haugh, St Andrews, Fife, KY16 9SS, UK*
[14]*Brorfelde Observatory, Observator Gyldenkernes Vej 7, DK-4340 Tølløse, Denmark*
[15]*DTU Space, National Space Institute, Technical University of Denmark, Elektrovej 327, DK-2800 Lyngby, Denmark*
[16]*Amateur Astronomer, Glendale, Arizona, USA*
[17]*Amateur Astronomer, 12812 SE 69th Place, Bellevue WA, USA*
[18]*Amateur Astronomer, 7507 52nd Pl NE, Marysville, WA, 98270, USA*
[19]*Citizen Scientist, c/o Zooniverse, Department of Physics, University of Oxford, Denys Wilkinson Building, Keble Road, Oxford, OX1 3RH, UK*
[20]*Citizen Scientist, Planet Hunter, Bottmingen, Switzerland*
[21]*Citizen Scientist, Planet Hunter, Petrozavodsk, Russia*
[22]*Department of Earth and Planetary Sciences, University of California, Riverside, CA 92521, USA*
[23]*Department of Physics, University of California, Santa Barbara, CA 93106-9530, USA*
[24]*SOTES Private Observatory, Suwalki, Poland*
[25]*WWVSH (World Wide Variable Star Hunters), Abu Dhabi, United Arab Emirates*
[26]*Villa '39 Observatory, Landers, CA 92285, USA*
[27]*Department of Physics and Kavli Institute for Astrophysics and Space Research, Massachusetts Institute of Technology, Cambridge, MA 02139, USA*
[28]*Department of Earth, Atmospheric and Planetary Sciences, Massachusetts Institute of Technology, Cambridge, MA 02139, USA*
[29]*Department of Aeronautics and Astronautics, MIT, 77 Massachusetts Avenue, Cambridge, MA 02139, USA*
[30]*Department of Astrophysical Sciences, Princeton University, 4 Ivy Lane, Princeton, NJ 08544, USA*
[31]*NASA Ames Research Center, Moffett Field, CA, 94035, USA*
[32]*NASA Goddard Space Flight Center, 8800 Greenbelt Road, Greenbelt, MD 20771, USA*
[33]*University of Maryland, Baltimore County, 1000 Hilltop Circle, Baltimore, MD 21250, USA*
[34]*SETI Institute, Mountain View, CA, 94043, USA*

Corresponding author: Andrew W. Mann
awmann@unc.edu

[35] *Department of Physics and Astronomy, University of New Mexico, 1919 Lomas Blvd NE, Albuquerque, NM 87131, USA*
[36] *Noqsi Aerospace Ltd., 15 Blanchard Avenue, Billerica, MA 01821, USA*

ABSTRACT

Exoplanets can evolve significantly between birth and maturity, as their atmospheres, orbits, and structures are shaped by their environment. Young planets (<1 Gyr) offer an opportunity to probe the critical early stages of this evolution, where planets evolve the fastest. However, most of the known young planets orbit prohibitively faint stars. We present the discovery of two planets transiting HD 63433 (TOI 1726, TIC 130181866), a young Sun-like ($M_* = 0.99 \pm 0.03$) star. Through kinematics, lithium abundance, and rotation, we confirm that HD 63433 is a member of the Ursa Major moving group ($\tau = 414 \pm 23$ Myr). Based on the TESS light curve and updated stellar parameters, we estimate the planet radii are $2.15 \pm 0.10 R_\oplus$ and $2.67 \pm 0.12 R_\oplus$, the orbital periods are 7.11 and 20.55 days, and the orbital eccentricities are lower than about 0.2. Using HARPS-N velocities, we measure the Rossiter-McLaughlin signal of the inner planet, demonstrating the orbit is prograde. Since the host star is bright (V=6.9), both planets are amenable to transmission spectroscopy, radial velocity measurements of their masses, and more precise determination of the stellar obliquity. This system is therefore poised to play an important role in our understanding of planetary system evolution in the first billion years after formation.

Keywords: exoplanets, exoplanet evolution, young star clusters- moving clusters, planets and satellites: individual (HD 63433)

1. INTRODUCTION

Over their lifetimes, the dynamical, structural, and atmospheric properties of planets are modified by their environment (e.g., Kaib et al. 2013; Ehrenreich et al. 2015) and internal processes (Fortney et al. 2011; Ginzburg et al. 2018). The simplest observational path to explore these processes is to compare the statistical properties of planets at different ages. Since the evolution is the most rapid in the first few hundred million years, planets with known ages <1 Gyr are especially useful.

With this in mind, the Zodiacal Exoplanets in Time Survey (ZEIT; Mann et al. 2016a), and its successor, the *TESS* Hunt for Young and Maturing Exoplanets (THYME; Newton et al. 2019) set out to identify transiting planets in young clusters, moving groups, and star-forming regions with ages of 5-700 Myr using light curves from the *K2* and *TESS* missions. Discoveries from these and similar surveys have found planets in diverse environments, from the 10-20 Myr Sco-Cen OB association (Rizzuto et al., in prep), to the 45 Myr Tucana-Horologium moving group (Newton et al. 2019; Benatti

et al. 2019), and as old as the 700 Myr Hyades cluster (Vanderburg et al. 2018). More importantly, these discoveries have demonstrated that young planets are systematically larger than older planets of the same mass (Obermeier et al. 2016; Mann et al. 2018) and that at least some short-period planets migrate within the first 10 Myr or form in situ (Mann et al. 2016b; David et al. 2016).

Studies of individual young systems can also be powerful, providing new insight into topics such as haze and cloud formation in young systems (e.g., Gao & Zhang 2020; Thao et al. 2020), photoevaporation and atmospheric escape (e.g., Gaidos et al. 2020, Rockcliffe et al. in prep), and exoplanet migration (e.g., Mann et al. 2016b; David et al. 2016). In particular, measurement of spin-orbit misalignments via the Rossiter-McLaughlin (RM) effect are important for young and multi-planet systems to inform our understanding of their dynamical histories. *TESS* has already enabled the discovery of young planets around bright stars (Newton et al. 2019), facilitating spin-orbit alignment measurements (Zhou et al. 2020; Montet et al. 2020).

Citizen scientists have long played an important role in the discovery of important planetary systems, particularly from *Kepler*, *K2*, and *TESS* mission data. This is in large part due to the success of programs like Planet Hunters (Schwamb et al. 2013; Wang et al. 2013) and Exoplanet Explorers (Christiansen et al. 2018). Young

planets are no exception; citizen scientists aided in the discovery and characterizing of both K2-25b ($\simeq$700 Myr, Mann et al. 2016a) and K2-233 (David et al. 2018, $\sim$400 Myr).

Despite these recent exoplanet discoveries, the sample of transiting planets with known, young ages is still small ($\simeq$ 30 planets), and most of them orbit stars too faint for follow-up with existing precision radial-velocity instruments (PRV). The sample is also heavily biased toward the extreme age ends of the survey, with most of the known planets at 700 Myr or <50 Myr (Mann et al. 2017; David et al. 2019).

We report the discovery of two young transiting planets, both with radii between $2R_\oplus$ and $3R_\oplus$. The host star (HD 63433) is a bright ($V \simeq 6.9$) member of the $\simeq$ 400 Myr Ursa Major Moving group. HD 63433 is the third-brightest star (by optical magnitude) discovered to host a transiting planet using *TESS* data; the only brighter stars so far are π Men (Huang et al. 2018) and HR 858 (Vanderburg et al. 2019).

In Section 2, we present the discovery data from *TESS*, as well as follow-up and archival photometry and spectroscopy used to characterize the planets and stellar host. In Section 3, we demonstrate HD 63433 is a member of Ursa Major and update the stellar parameters (radius, mass, $T_{\rm eff}$, age, and rotation). We fit the *TESS* transit data and Rossiter-McLaughlin (RM) velocities to provide parameters of both planets, which we discuss in Section 4. We detail our validation of the signals as planetary in origin in Section 5 and discuss its dynamical stability in Section 6. We conclude in Section 7 with a brief summary and discussion of future follow-up of HD 63433bc and of the Ursa Major cluster more generally.

2. OBSERVATIONS

2.1. *TESS Photometry*

The *TESS* mission (Ricker et al. 2014) observed TIC 130181866 (TOI 1726, HD 63433, HIP 38228) between 2019 December 24 and 2020 January 21 (Sector 20) using Camera 1. The target was proposed by three guest investigator programs (G022032, T. Metcalfe; G022038, R. Roettenbacher; G022203, J. Ge) and hence has has 2-minute cadence data. The abstracts for these GI programs suggest HD 63433 was targeted because it is bright ($V \simeq 7$ mag) and/or active.

For our analysis, we used the Presearch Data Conditioning simple aperture photometry (PDCSAP; Smith et al. 2012; Stumpe et al. 2014) *TESS* light curve produced by the Science Process Operations centre (SPOC; Jenkins et al. 2016) and available through the Mikul-

ski Archive for Space Telescopes (MAST)[1]. We only included data points with `DQUALITY=0`, i.e., those with no flags from the SPOC pipeline. No obvious flares were present in the data, so we did no further data processing.

2.2. *Ground-Based Photometry*

We obtained time-series photometry during three predicted transits of HD 63433 b using ground-based facilities in order to rule out nearby eclipsing binaries (NEBs) which could be the source of the transit signal. We observed an egress on 2020 February 22 UT, and a full transit on 2020 February 29, both in r with the 0.6 m World Wide Variable Star Hunters (WWVSH) telescope in Abu Dhabi, United Arab Emirates. Both transits were observed under clear (near-photometric) conditions. The telescope is equipped with a Finger Lakes Instrumentation FLI 16803 camera, giving a pixel scale of 0.47" pixel^{-1}. We obtained 118 and 350 exposures with an exposure length of 180 and 90 seconds for the two observations, respectively. We also observed a full transit of the 2020 February 29 event with one of the 1 m telescopes at the Las Cumbres Observatory (LCOGT; Brown et al. 2013) node at the South African Astronomical Observatory, South Africa under clear conditions. We observed in the z_s band using a Sinistro camera, giving a pixel scale of 0.389" pixel^{-1}. We obtained 161 60-second exposures, which were reduced using the BANZAI pipeline (McCully et al. 2018). In all cases, we deliberately saturated the target star in order to search for faint NEBs.

We performed aperture photometry on all three datasets using the `AstroImageJ` package (AIJ; Collins et al. 2017). TIC 130181879 (*TESS* magnitude 13.1) and TIC 130181877 (*TESS* magnitude 14.6) are the only two stars within 2.5′ of HD 63433 that are bright enough to cause the *TESS* detection, so we extracted light curves for both. We used the aperture size and set of comparison stars that yielded the best precision for each observation and star of interest. For both WWVSH observations, we used a 7-pixel (3.3″) radius circular aperture to extract the source and an annulus with a 12-pixel (5.6″) inner radius and a 17-pixel (8″) outer radius for the sky. For the LCO photometry, we used a 6-pixel (2.3″) radius circular aperture for the source and a annulus with a 16-pixel (6.2″) inner radius and a 23-pixel (9″) outer radius for the sky. For all observations, we centered the apertures on the source, weighted all pixels within the aperture equally, and used the same aper-

---

[1] https://mast.stsci.edu/portal/Mashup/Clients/Mast/Portal.html

ture setup for TIC 130181879 and TIC 130181877. The
extracted light curves (including for additional nearby
faint sources), field overlays, and further information on
this follow-up can be found on on ExoFOP-TESS[2].

To reproduce the observed transit depths, eclipses
around either nearby star would need to be large
($\simeq$20%), but no binary was detected down to $\lesssim$ 1%.
Thus, the observations ruled out any NEB scenario con-
sistent with the observed transit.

2.3. *Spectroscopy*

We utilized new and archival high-resolution spectra
and radial velocity measurements of HD 63433 in our
analysis. We list all of the radial velocity data in Ta-
bles 1 and 2.

2.3.1. *LCOGT/NRES*

We obtained three spectra of HD 63433 using the
LCOGT Network of Robotic Echelle Spectrographs
(NRES; Siverd et al. 2018) between 2020 Feb. 26
and Mar. 3 UT. All observations were taken under
thin cloud-cover or clear conditions, using an exposure
time of 900 seconds with the NRES unit at the Wise
Observatory, Israel. NRES is a set of four identical
cross-dispersed echelle spectrographs which are fiber-
fed by 1 m telescopes in the LCOGT network. NRES
provides a resolving power of $R = 53,000$ over the
range $3800 - 8600$ Å. The spectra were reduced, ex-
tracted, and wavelength calibrated using the standard
NRES pipeline[3]. We measured radial velocities from
the spectra using cross-correlation within the NRES
Stage2 pipeline, and measured stellar parameters from
the SpecMatch-Synth code[4]. The NRES spectra show
no significant radial velocity shift between epochs, and
no evidence of double lines or other indications of a false
positive.

2.3.2. *Tillinghast/TRES*

We obtained two spectra of HD 63433 with the
1.5m Tillinghast Reflector and the Tillinghast Reflec-
tor Echelle Spectrograph (TRES; Fűrész 2008) located
at Fred Lawrence Whipple Observatory, Arizona, USA.
TRES is a cross-dispersed echelle spectrograph and de-
livers a resolving power of $R = 44,000$ over the range
$3900 - 9100$ Å. We obtained one spectrum each on 2020
February 21 and 24 UT, near opposite quadratures of
the orbit of HD 63433 b.

Table 1. Radial Velocity Measurements of HD 63433

BJD	v (km s^{-1})[a]	σ_v (km s^{-1})[b]	Instrument
2450510.3603	-15.798	0.023	ELODIE
2450511.4079	-15.831	0.023	ELODIE
2451984.308	-15.851	0.023	ELODIE
2456945.67006	-15.811	0.002	SOPHIE
2457102.36074	-15.817	0.002	SOPHIE
2457099.37892	-15.757	0.002	SOPHIE
2457059.53146	-15.847	0.003	SOPHIE
2457492.3052	-15.841	0.002	SOPHIE
2457490.30522	-15.858	0.002	SOPHIE
2457448.41586	-15.854	0.002	SOPHIE
2457444.45015	-15.774	0.002	SOPHIE
2456386.31072	-15.846	0.001	SOPHIE
2456388.34133	-15.774	0.001	SOPHIE
2456390.3025	-15.871	0.002	SOPHIE
2456383.32005	-15.863	0.003	SOPHIE
2456388.29898	-15.777	0.002	SOPHIE
2450831.81836	0.021	0.008	Hamilton
2450854.79102	-0.009	0.009	Hamilton
2451469.00303	-0.007	0.005	Hamilton
2453014.84277	0.040	0.006	Hamilton
2453033.81543	-0.006	0.005	Hamilton
2453068.72168	0.011	0.006	Hamilton
2453388.79327	-0.012	0.005	Hamilton
2453390.88716	0.003	0.005	Hamilton
2454783.95126	-0.046	0.006	Hamilton
2454865.81449	0.031	0.005	Hamilton
2455846.99256	-0.016	0.006	Hamilton
2458900.693564	-15.838	0.028	TRES
2458903.822341	-15.867	0.028	TRES
2458906.27953	-15.740	. . .	NRES
2458908.21348	-16.060	. . .	NRES
2458912.24069	-16.110	. . .	NRES

[a] The Hamilton (Lick) radial velocities are relative, whereas the
other radial velocities are on an absolute frame (although
instrumental offsets may still be present).

[b] RV errors are likely underestimated due to missing terms (e.g.,
from stellar jitter). The NRES pipeline does not currently
estimate radial velocity
uncertainties.

We reduced the TRES data and derived radial ve-
locities using the standard TRES pipeline as described
in (Buchhave et al. 2010). We cross-correlated the ex-
tracted spectrum against a rotating synthetic spectrum
with parameters similar to HD 63433. For this, we used
all 21 orders of the TRES spectrum, spanning 4140–
6280Å, only avoiding regions of high telluric contamina-
tion and variable features (e.g. Balmer lines). We then
determined the instrumental noise floor from nightly ob-
servations of bright radial velocity standard stars and
added this uncertainty in quadrature with the internal
error estimates (derived from the variation between or-
ders). To ensure our velocities are on the absolute scale
from Nidever et al. (2002), we used the values derived

Table 2. HARPS-N Rossiter-McLaughlin Velocity Measurements

BJD	v (km s^{-1})	σ_v (km s^{-1})
2458916.36135	-15.7481	0.0017
2458916.36645	-15.7495	0.0014
2458916.37178	-15.7477	0.0013
2458916.37670	-15.7467	0.0014
2458916.38178	-15.7478	0.0013
2458916.38684	-15.7460	0.0015
2458916.39180	-15.7444	0.0016
2458916.39972	-15.7451	0.0019
2458916.41321	-15.7448	0.0012
2458916.41813	-15.7415	0.0013
2458916.42337	-15.7455	0.0016
2458916.42875	-15.7434	0.0017
2458916.43361	-15.7439	0.0016
2458916.43867	-15.7454	0.0016
2458916.44392	-15.7447	0.0016
2458916.44898	-15.7500	0.0017
2458916.45424	-15.7472	0.0019
2458916.45942	-15.7453	0.0018
2458916.46442	-15.7481	0.0019
2458916.46953	-15.7492	0.0020
2458916.47516	-15.7471	0.0017
2458916.48009	-15.7482	0.0016
2458916.48524	-15.7474	0.0019
2458916.49000	-15.7485	0.0022
2458916.49554	-15.7475	0.0020
2458916.50089	-15.7479	0.0020
2458916.50599	-15.7490	0.0021
2458916.51085	-15.7474	0.0015
2458916.51611	-15.7481	0.0018
2458916.52145	-15.7463	0.0020
2458916.52641	-15.7463	0.0017
2458916.53135	-15.7450	0.0020
2458916.53688	-15.7433	0.0017
2458916.54188	-15.7458	0.0014
2458916.54691	-15.7432	0.0014
2458916.55229	-15.7480	0.0015
2458916.55738	-15.7481	0.0015
2458916.56268	-15.7470	0.0014
2458916.56791	-15.7451	0.0015
2458916.57300	-15.7463	0.0014
2458916.57768	-15.7467	0.0014
2458916.58336	-15.7472	0.0016
2458916.58844	-15.7470	0.0014

from the Mg b order (5190Å) and applied an offset to account for the difference between standard star radial velocities determined in an identical manner and the velocities reported by Nidever et al. (2002) for the same standards. The uncertainty in shifting to this absolute scale (and of the scale itself) is of order 0.1 km/s; errors on relative velocities are 0.028 km/s. Like the NRES data, the TRES spectra show no evidence of large velocity shifts or multiple lines that could indicate a binary.

2.3.3. Goodman/SOAR

To aid our spectral-energy-distribution fits (Section 3.2), we obtained spectra of HD 63433 with the Goodman High-Throughput Spectrograph (Clemens et al. 2004) on the Southern Astrophysical Research (SOAR) 4.1 m telescope located at Cerro Pachón, Chile. On 2020 March 6 (UT) and under photometric conditions, we took five spectra of HD 63433, each with an exposure time of 5s using the red camera, the 1200 l/mm grating in the M5 setup, and the 0.46″ slit rotated to the parallactic angle. This setup yielded a resolving power of $R \simeq 5900$ spanning 6250–7500Å. For calibration, we obtained Ne arc lamps taken throughout the night (to account for drifts in the wavelength solution), as well as standard calibration data (dome/quartz flats and biases) taken during the afternoon.

We performed bias subtraction, flat fielding, optimal extraction of the target spectrum, and found the wavelength solution using a 4th-order polynomial derived from the Ne lamp data. We then stacked the five extracted spectra using the robust weighted mean (for outlier removal). The stacked spectrum had a signal-to-noise ratio of $200 - 300$ over the full wavelength range.

2.3.4. HARPS-N/TNG

With the aim of detecting the Rossiter-McLaughlin (RM) effect, we observed HD 63433 during the predicted transit of planet b on the night of 2020 March 7/8 (UT), under photometric conditions, with the High Accuracy Radial velocity Planet Searcher for the Northern hemisphere (HARPS-N; Cosentino et al. 2012, 2014) spectrograph installed at the Telescopio Nazionale Galileo (TNG) at the Roque de los Muchachos Observatory on La Palma, Canary Islands, Spain. HARPS-N is a high-resolution (R≃120,000) spectrograph encased in a vacuum vessel that controls temperature and pressure at levels required for <1 m s^{-1} instrumental drifts. To cover both the transit and at least 1h of out-of-transit baseline, we took 43 spectra, spanning 5.4h in total and each with a fixed exposure time of 420s.

Radial velocities were extracted from the HARPS-N spectra with the standard pipeline that uses a weighted cross-correlation with the numerical mask matching the spectral type (G2) of the target (Pepe et al. 2002). Typical radial velocity uncertainties were between 1–3 m s^{-1}.

2.4. Archival Velocities

Between 1997 March and 2016 April, HD 63433 was observed 15 times from the 1.93m telescope at the Haute-Provence Observatory located in France. The first three were taken with the ELODIE high-resolution spectrograph (Baranne et al. 1996) and the next 12 were taken by ELODIE's replacement, SOPHIE (Perruchot et al. 2008). We retrieved the spectra and barycentric

radial velocities given on the SOPHIE/ELODIE archives (Moultaka et al. 2004)[5]. To correct for differences in the zero-point between ELODIE and SOPHIE, we apply an offset of $87\pm23\,\mathrm{m\,s^{-1}}$ to ELODIE velocities as described in Boisse et al. (2012). SOPHIE velocities were all taken after the upgrade to SOPHIE+ (Bouchy et al. 2013) and have formal uncertainties of $1\text{-}3\,\mathrm{m\,s^{-1}}$, not including stellar jitter or long-term drift in the instrument ($\simeq 5\,\mathrm{m\,s^{-1}}$; Courcol et al. 2015).

As part of the Lick planet search program HD 63433 was observed 11 times between 1998 January and 2011 December using the Hamilton Spectrograph and iodine cell (Vogt 1987) at Lick Observatory in California, USA. We utilize the velocities and errors reported in Fischer et al. (2014). Velocity errors from the Lick planet search include instrument stability, but do not account for stellar jitter. These are relative velocities (the star compared to itself) and hence cannot be directly compared to other measurements without modeling an offset (Díaz et al. 2016).

3. HOST STAR ANALYSIS

We summarize constraints on the host star in Table 3, the details of which we provide in in this section.

3.1. *Membership to Ursa Major and Age*

The Ursa Major Group (UMaG) has long been proposed as a kinematically similar grouping of stars (e.g., Proctor 1869; Rasmuson 1921; Eggen 1965) centered on several of the stars comprising the Ursa Major constellation. While UMaG has a clear core of members that are homogeneous in kinematics and color-magnitude-diagram position (Soderblom & Mayor 1993; King et al. 2003), many associations with large spatial distributions have turned out to be larger star-formation events with multiple ages (e.g., Sco-Cen and Taurus-Auriga, Rizzuto et al. 2011; Kraus et al. 2017). Further, the spatial spread of UMaG members outside the core leads to a large number of interloping stars with similar Galactic orbits, but different ages. Tabernero et al. (2017) found that $\simeq 2/3$ of UMaG members have similar chemical compositions, suggesting either multiple stellar populations or a large fraction of contaminants in the membership list. Thus, to be useful for age-dating HD 63433, we need to establish its association to the core members of UMaG using both kinematics and independent metrics (e.g., rotation and abundances).

UMaG has recent age estimates ranging from 390-530 Myr (e.g., David & Hillenbrand 2015; Brandt &

Table 3. Properties of the host star HD 63433.

Parameter	Value	Source
Astrometry		
α.	07:49:55.06	*Gaia* DR2
δ.	+27:21:47.5	*Gaia* DR2
μ_α (mas yr^{-1})	-10.027±0.085	*Gaia* DR2
μ_δ (mas yr^{-1})	-11.314±0.049	*Gaia* DR2
π (mas)	44.607±0.044	*Gaia* DR2
Photometry		
G$_{Gaia}$ (mag)	6.7183±0.0005	*Gaia* DR2
BP$_{Gaia}$ (mag)	7.0919±0.0021	*Gaia* DR2
RP$_{Gaia}$ (mag)	6.2322±0.0022	*Gaia* DR2
B$_T$ (mag)	7.749 ± 0.016	Tycho-2
V$_T$ (mag)	6.987 ± 0.010	Tycho-2
J (mag)	5.624 ± 0.043	2MASS
H (mag)	5.359 ± 0.026	2MASS
Ks (mag)	5.258 ± 0.016	2MASS
W1 (mag)	5.246 ± 0.178	ALLWISE
W2 (mag)	5.129 ± 0.087	ALLWISE
W3 (mag)	5.297 ± 0.016	ALLWISE
W4 (mag)	5.163 ± 0.031	ALLWISE
Kinematics & Position		
RV$_{\mathrm{Bary}}$ (km s^{-1})	-15.81±0.10	This paper
U (km s^{-1})	13.66±0.09	This paper
V (km s^{-1})	2.42±0.02	This paper
W (km s^{-1})	-7.75±0.04	This paper
X (pc)	-19.89±0.02	This paper
Y (pc)	-4.697±0.005	This paper
Z (pc)	9.164±0.091	This paper
Physical Properties		
P_{rot} (days)	6.45 ± 0.05	This paper
L_X/L_{bol}	$(9.1 \pm 2.7) \times 10^{-5}$	This paper
$\log R'_{\mathrm{HK}}$	-4.39 ± 0.05	This paper
$v \sin i_*$ (km s^{-1})	7.3 ± 0.3	This paper
i_* ($^\circ$)	> 74	This paper
F_{bol} (erg cm^{-2} s^{-1})	$(4.823 \pm 0.12) \times 10^{-8}$	This paper
T$_{\mathrm{eff}}$ (K)	5640 ± 74	This paper
M$_\star$ (M$_\odot$)	0.99 ± 0.03	This paper
R$_\star$ (R$_\odot$)	0.912 ± 0.034	This paper
L$_\star$ (L$_\odot$)	0.753 ± 0.026	This paper
$\rho_\star$ ($\rho_\odot$)	1.3 ± 0.15	This paper
Age (Myr)	414 ± 23	Jones et al. (2015)

Huang 2015). Direct radius measurements from long-baseline interferometry for the A stars in UMaG point toward a common age of $\tau = 414 \pm 23$ Myr (Jones et al. 2015). We adopt this measurement as the cluster age for analyses in this paper.

HD 63433 was first identified as a possible member of UMaG by Gaidos (1998) based on its kinematics and X-ray luminosity, and has since been included as a candidate or likely member in multiple analyses (e.g., King et al. 2003; Fuhrmann 2008; Vereshchagin et al. 2018). The spatial and kinematic definition of UMaG was most recently updated by Gagné et al. (2018), who identified central values of $(X, Y, Z) = (-7.5, +9.9, +21.9)$ pc and $(U, V, W) = (+14.8, +1.8, -10.2)$ km s^{-1}, along with

full covariance matrices for these parameters. These are marginally consistent with the central values from Mamajek et al. (2010) of $(U, V, W) = (+15.0, 2.8, -8.1)$ $\pm$ (0.4, 0.7, 1.0) km s^{-1}. The Gaia DR2 proper motion, parallax, and our radial velocity for HD 63433 give $(U, V, W) = (+13.66, +2.42, -7.75)$ km s^{-1}. Following the method from Gagné et al. (2018)[6], we calculate a membership probability of $P_{mem} = 99.98\%$ using the Gagné et al. (2018) space velocity for UMaG, and $P_{mem} = 95\%$ using the space velocity from Mamajek et al. (2010).

HD 63433's Galactic position of $(X, Y, Z) = (-19.89, -4.70, 9.16)$ pc is 23 pc from the core of UMaG at $(X, Y, Z) = (-7.5, 9.9, 21.9)$ pc. While the core members of UMaG are within $\simeq 4$ pc of the core, more than half of known members >20 pc away (Madsen et al. 2002). The large-scale velocity dispersion is $\simeq 1$ km s^{-1} ($\simeq 1$ pc/Myr) and the age is $\tau \sim 400$ Myr; members could easily be spread over >100 pc in Y (where orbits can freely diverge) and a still substantial distance even in X and Z (where epicyclic motion prevent the spatial distribution from broadening to the same degree). Mamajek et al. (2010) and Schlieder et al. (2016) argue that the measured dispersion of $\simeq 1$ km s^{-1} is mostly an artifact of including spectroscopic binaries in the sample, and that the true dispersion is smaller. However, given the age of the cluster, HD 63433 only needs to have a velocity difference of $\simeq 0.06$km s^{-1} to explain a 23 pc separation. It is more likely that the velocity difference is larger and HD 63433 was evaporated from the cluster core in the last 100 Myr.

The photospheric lithium abundance provides an age and membership diagnostic that is independent of the 6D position-velocity phase space of HD 63433. Li is destroyed at temperatures common to the cores of stars ($\sim 2.5 \times 10^6$ K), which slowly depletes surface Li at a rate that depends on the core-surface transport efficiency (e.g., convection). While there is significant scatter within a single age group (e.g., Somers & Pinsonneault 2015), there is still a shift in the average A(Li)-$T_{\rm eff}$ sequence with age.

We compared the A(Li) abundance of HD 63433 from Ramírez et al. (2012) to A(Li) for members of Pleiades (125 Myr; Dahm 2015) and Hyades (700 Myr; Martín et al. 2018). A(Li) measurements for the Pleiades were taken from Bouvier et al. (2018), and values for the Hyades from Boesgaard et al. (2016). We also considered UMaG members that were confirmed using kinematics and chromospheric activity by King et al.
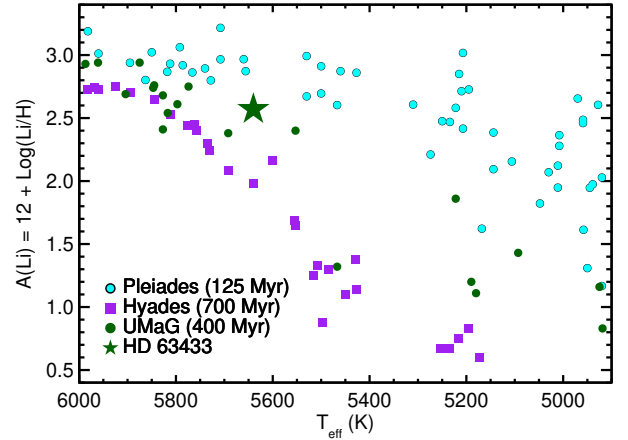
Figure 1. A(Li) sequence as a function of $T_{\rm eff}$ for Hyades (purple), Pleiades (cyan) and UMaG (green). UMaG lands in between the two clusters, as expected for its intermediate age. HD 63433 is shown as a green star; its A(Li) abundance is within the expected sequence for UMaG between Hyades and Pleiades.

(2003). We retrieved A(Li) from King & Schuler (2005), Ramírez et al. (2012), Aguilera-Gómez et al. (2018), and the Hypatia catalog (Hinkel et al. 2014). HD 63433 has A(Li) between that of Hyades and Pleiades stars of similar $T_{\rm eff}$, and is consistent with the core members of UMaG, furthering the case for membership (Figure 1).

Stellar rotation provides an additional check on the age and membership of HD 63433. Once on the main sequence, young stars lose angular momentum with time, decreasing their rotation periods. After 100-600 Myr, Sun-like stars eventually converge to a sequence (van Saders et al. 2016; Douglas et al. 2016). Angus et al. (2015) used this information to provide a calibration between $B - V$, $P_{\rm rot}$, and age, which predicts a rotation period of 6.9 ± 0.4 d for HD 63433 if it is a member of UMaG.

We estimated the rotation period of HD 63433 and other likely UMaG members from their *TESS* or *K*2 light curves using a combination of the Lomb-Scargle periodogram following Horne & Baliunas (1986) and the autocorrelation function as described in McQuillan et al. (2013). For this, we used the simple-aperture-photometry (SAP) lightcurves, as PDCSAP curves tend to have long-term signals removed or suppressed (e.g., Smith et al. 2012; Van Cleve et al. 2016). For HD 63433, this yielded a period estimate of 6.45 d (Figure 2). The Lomb-scargle power is relatively broad, although the power is high and bootstrap re-sampling of the light curve suggest on this period of $\lesssim 3\%$. Our derived period is also consistent with the literature estimate of 6.46 ± 0.01 d from Gaidos et al. (2000). Rotation periods

Table 4. Rotation Periods for likely Members of UMaG

Object	TIC	RA	Dec	Bp-Rp	Prot
		(deg)	(deg)	(mag)	(days)
HD109011	316331312	187.82883	55.11897	1.193	8.40
HD109647	224305606	188.96370	51.22148	1.180	4.57
HD109799	60709182	189.42616	-27.13888	0.468	0.79
HD110463	99381773	190.43551	55.72467	1.165	12.07
HD11131	24910401	27.34729	-10.70362	0.804	9.16
HD111456	142277151	192.16436	60.31973	0.665	1.47
HD11171	24910738	27.39626	-10.68641	0.456	0.76
HD113139A	229534764	195.18163	56.36633	0.515	0.73
HD115043	157272202	198.40420	56.70827	0.789	5.53
HD147584	362747897	247.11725	-70.08440	0.725	8.22
HD165185	329574145	271.59883	-36.01979	0.780	5.90
HD180777	235682463	287.29116	76.56050	0.433	0.77
HD238224	159189482	200.84697	57.90606	1.657	12.13
HD26923	283792884	63.87000	6.18686	0.747	5.78
HD38393	93280676	86.11580	-22.44838	0.720	12.89
HD59747	16045498	113.25242	37.02985	1.059	7.94
HD63433	130181866	117.47942	27.36318	0.860	6.39
HD72905	417762326	129.79877	65.02091	0.800	4.95
HD95650	97488127	165.65976	21.96714	2.015	13.75

for other likely members are listed in Table 4. We note that because of the narrow window provided by *TESS* photometry for many UMaG members (<30 d), our estimates are subject to aliasing (i.e., true periods may be double or half the assigned value) separate from the smaller formal errors ($\simeq 3\%$).

As with A(Li), we compare our UMaG rotation periods to those from the older Praesepe cluster (from Douglas et al. 2019) and younger Pleiades cluster (from Rebull et al. 2016). We show the results in Figure 3. There is significant scatter in each sequence (e.g., from binarity and non-member interlopers). The UMaG sequence lands just below the Praesepe sequence in period space, and most members are above (longer periods) than the Pleiades sequence. As expected, HD 63433 follows the overall trend for UMaG. The rotation sample considered here is small, and a more complete accounting of UMaG membership is needed to explore the overlap between Praesepe and UMaG rotation sequences.

Altogether, the available evidence confirms the age and membership of HD 63433. For all analyses in the rest of the paper, we adopt the cluster age (414 ± 23 Myr) as the age of HD 63433.

3.2. *Spectral Energy Distribution Fit*

We fit HD 63433's spectral-energy-distribution using available photometry, our Goodman optical spectrum (Section 2.3.3), and spectral templates of nearby stars (e.g., Rayner et al. 2009; Falcón-Barroso et al. 2011). To this end, we followed the basic methodology of Mann

et al. (2015). The procedure gives precise (1-5%) estimates of $F_{\rm bol}$ from the integral of the absolutely calibrated spectrum, L_* from $F_{\rm bol}$ and the *G*aia distance, and $T_{\rm eff}$ from comparing the calibrated spectrum to atmospheric models. This method reproduces angular diameter measurements from long-baseline optical interferometry (e.g., von Braun et al. 2012). As a check, the same procedure also provides an estimate of R_* from the infrared-flux method (Blackwell & Shallis 1977), i.e., the ratio of the absolutely calibrated spectrum to the model spectrum is R_*^2/D^2 (also see Equation 1 of Cushing et al. 2008).

We first combined our template and observed spectra with Phoenix BT-SETTL models (Allard et al. 2011) to cover wavelength gaps and regions of high telluric contamination and assumed a Rayleigh-Jeans law redward of where the models end (25-30μm). To absolutely calibrate the combined spectra, we used literature optical and NIR photometry from the Two-Micron All-Sky Survey (2MASS; Skrutskie et al. 2006), the Wide-field Infrared Survey Explorer (WISE; Cutri & et al. 2014), *G*aia data release 2 (DR2; Evans et al. 2018; Lindegren et al. 2018), AAVSO All-Sky Photometric Survey (APASS; Henden et al. 2016), Tycho-2 (Høg et al. 2000), Hipparcos (van Leeuwen et al. 1997), and the General Catalogue of Photometric Data (Mermilliod et al. 1997). To account for variability of the source, we assumed all photometry had an addition error of 0.02 mag (for optical) or 0.01 mag (for near-infrared), and filter zero-points are assumed to have errors of 0.015 mag unless a value is given in the source. We then compared the literature photometry to synthetic magnitudes derived from combined spectrum using the relevant filter profiles and zero points (e.g., Mann & von Braun 2015; Maíz Apellániz & Weiler 2018). We assumed no reddening, as HD 63433 lands within the local bubble (Sfeir et al. 1999). In addition to the overall scale of the spectrum, there are four free parameters of the fit that account for imperfect (relative) flux calibration of the spectra and both the model and template spectra used.

We show the best-fit spectrum and photometry in Figure 4. There is no significant NIR excess seen out to $W4$, consistent with most stars at this age (Cieza et al. 2008). Our joint fitting procedure yielded $T_{\rm eff}=5640 \pm 71$ K, $F_{\rm bol}=4.823 \pm 0.12 \times 10^{-8}$ erg cm^{-2} s^{-1}, $L_* = 0.753 \pm 0.026\,L_\odot$, and $R_* = 0.912 \pm 0.034 R_\odot$. Our derived $T_{\rm eff}$ is $< 1\sigma$ consistent with literature determinations using high-resolution spectra (5600–5700 K; Baumann et al. 2010; Ramírez et al. 2012; Luck 2017) and all parameters match our model interpolation below.

Version 8 of the *TESS* Input Catalog (TICv8; Stassun et al. 2018, 2019) lists stellar parameters of $T_{\rm eff}=5693\pm$
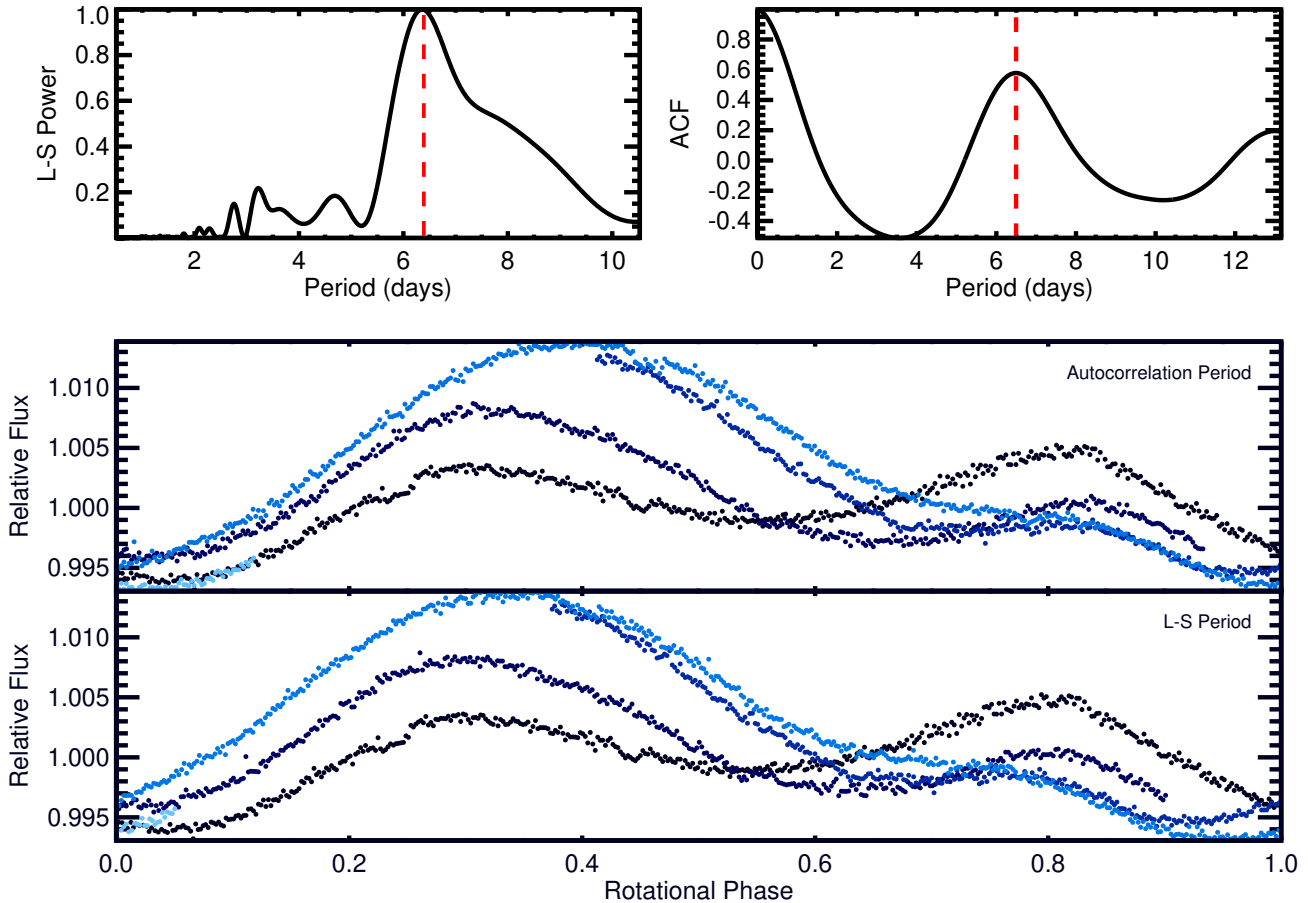
Figure 2. Diagnostic plot of our rotation period estimate for HD 63433. The top two panels show the Lomb-Scargle (left) and autocorrelation (right) power, with dashed lines indicating the assigned period. The bottom two panels show the *TESS* light curve phase-folded to the two periods from Lomb-Scargle (bottom) and the autocorrelation function (middle).

153 K, [Fe/H]= 0.017 ± 0.017, $R_* = 0.903\pm0.055R_\odot$, and $L_* = 0.772 \pm 0.020L_\odot$. These are all in $\simeq 1\sigma$ agreement with our SED-based parameters.

3.3. *Spectroscopic Classification*

We derived spectral parameters from the TRES spectra of HD 63433 using the Spectral Parameter Classification (SPC) tool (Buchhave et al. 2012). SPC cross correlates the observed spectrum against a grid of synthetic spectra based on Kurucz atmospheric models (Kurucz 1993). $T_{\rm eff}$, *log g* , bulk metallicity ([M/H]), and $v\sin i_*$ are allowed to vary as free parameters. This yielded $T_{\rm eff}$= 5705 ± 50 K, *log g* = 4.59 ± 0.10, [M/H]= -0.09 ± 0.08.

We ran a similar analysis using the HARPS-N stacked spectrum with ARES/MOOG following Sousa et al. (2015). Including empirical corrections from Sousa et al. (2011) and Mortier et al. (2014) yielded $T_{\rm eff}$=5764 $\pm$ 73 K, *log g* = 4.65 ± 0.12 and [Fe/H]= 0.04 ± 0.05.

Both methods were consistent with our $T_{\rm eff}$ derived using the SED, and the metallicity esitmates agrees with

the established value for UMaG (-0.03 ± 0.05; Ammler-von Eiff & Guenther 2009).

3.4. *Evolutionary-model parameters*

To determine the mass of HD 63433, we used Mesa Isochrones and Stellar Tracks (MIST; Choi et al. 2016). We compared all available photometry to the model-predicted values, accounting for errors in both the photometric zero-points and stellar variability as in Section 3.2. We restrict the comparison to 300–600 Myr and solar metallicity based on the properties of the cluster. We assumed Gaussian errors on the magnitudes, but included a free parameter to describe underestimated uncertainties in the models or data. The best-fit parameters from the MIST models were $M_* = 0.991\pm0.027M_\odot$, $R_* = 0.895 \pm 0.021R_\odot$, $T_{\rm eff}$=5690$\pm$61 K, and $L_* = 0.784 \pm 0.031L_\odot$. These are consistent with our other determinations, but we adopt our empirical L_*, $T_{\rm eff}$ and R_* estimates from the SED and only utilize the M_* value from the evolutionary models in our analysis.
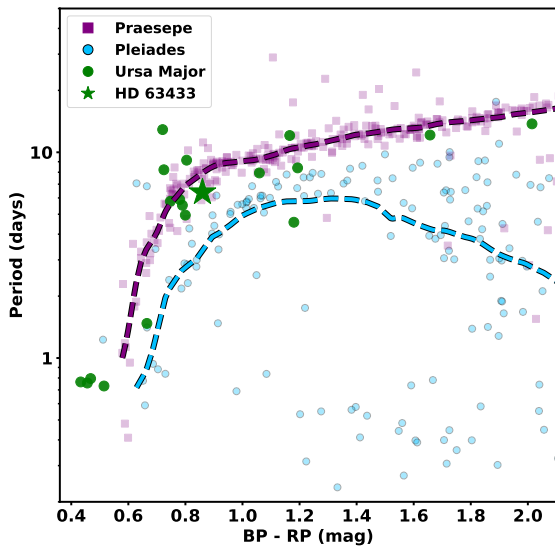
Figure 3. Rotation period versus *Gaia* $BP - RP$ color for members of the $\simeq 700$ Myr Praesepe clusters (purple), $\simeq 125$ Myr Pleiades cluster (cyan), and $\simeq 400$ Myr UMaG (green). HD 63433 is shown as a green star. For clarity, we also show a running median excluding stars with <0.2 day rotation periods for Praesepe and Pleiades (dashed lines). While there is significant scatter and overlap between all three distributions, HD 63433 matches the sequence expected for UMaG's assigned age.

3.5. *Stellar Inclination*

Using the combination of projected rotation velocity ($v \sin i_*$), $P_{\rm rot}$, and R_*, we can estimate the stellar inclination (i_*), and hence test if the stellar spin and planetary orbit are consistent with alignment. In principle, this is done by estimating the V term in $v \sin i_*$ using $V = 2\pi R_*/P_{\rm rot}$, although in practice it requires additional statistical corrections, including the fact that we can only measure alignment projected onto the sky. To this end, we follow the formalism from Masuda & Winn (2020), which handles the hard barrier at $i_* > 90°$ by rewriting the relation in terms of $\cos(i)$.

We used our $P_{\rm rot}$ from Section 3.1 estimated from the *TESS* light curve, and our R_* derived in Section 3.2. HD 63433 has $v \sin i_*$ measurements from a range of literature sources, with estimates from 7.0 km s^{-1} (Marsden et al. 2014) to 7.7 km s^{-1} (Luck 2017). Our fit of the TRES spectra yielded a consistent estimate of $v \sin i_* = 7.3 \pm 0.3$ km s^{-1} with a macroturbulent velocity of 4.2 ± 1.2 km s^{-1} and the SpecMatch run on the NRES spectra yielded 7.1 ± 0.3 km s^{-1}. We adopted 7.3 ± 0.3 km s^{-1}, which encompassed all estimates.
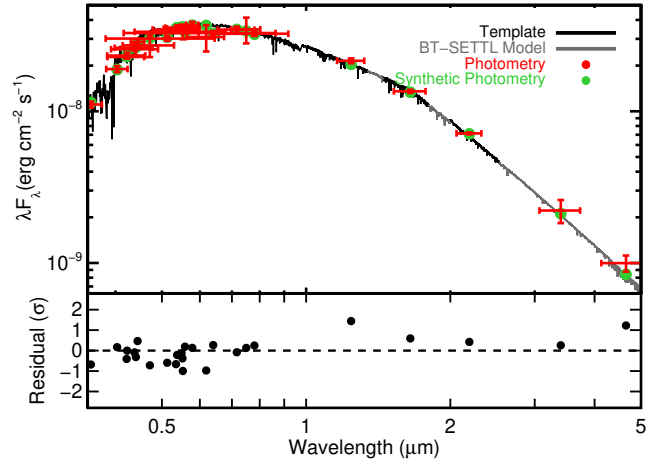
Figure 4. Best-fit spectral template and Goodman spectrum (black) compared to the photometry of HD 63433. Grey regions are BT-SETTL models, used to fill in gaps or regions of high telluric contamination. Literature photometry is shown in red, with horizontal errors corresponding to the filter width and vertical errors to the measurement errors. Corresponding synthetic photometry is shown as green points. The bottom panel shows the residuals in terms of standard deviations from the fit.

The combined parameters yielded a equatorial velocity (V) of 7.16 ± 0.29 km s^{-1} and a lower limit for the inclination of $i_* > 74°$ at 68% confidence and $i > 58°$ at 95% confidence. This is consistent with the stellar rotation being aligned with the planetary orbits ($i \simeq 90°$).

3.6. *Limits on Bound, Spatially Resolved Companions*

HD 63433 has adaptive optics or interferometric data spanning almost a decade, from 1999 (Mason et al. 2001a) to 2008 (Raghavan et al. 2012). The deepest extant high-resolution imaging reported in the literature for HD 63433 was obtained with the NaCo instrument at the VLT on 2004 Jan 16 UT (Program 072.C-0485(A); PI Ammler). The observation consisted of a series of individual 35 sec exposures, totaling 980 sec in all, taken with the K_s filter and with the central star behind a 0.7″ opaque Lyot coronagraph. The results of these observations were reported by Ammler-von Eiff et al. (2016), who found no candidate companions within $\rho < 9″$. The detection limits were reported in a figure in that work, and achieved contrasts of $\Delta K_s \sim 7$ mag at 0.5″, $\Delta K_s \sim 9$ mag at 1″, $\Delta K_s \sim 11$ mag at 2″, and $\Delta K_s \sim 13$ mag at $\geq 3″$. Given an age of $\tau \sim 400$ Myr, the evolutionary models of Baraffe et al. (2015) would imply corresponding physical limits of $M < 65 M_{Jup}$ at $\rho \sim 11$ AU, and $M < 50 M_{Jup}$ at $\rho > 22$ AU.

Mason et al. (2001b) and Raghavan et al. (2012) reported null detections at higher spatial resolution using speckle and long-baseline interferometry. These obser-

vations are consistent with the limits set by the lack of Gaia excess noise as indicated by the Renormalized Unit Weight Error (Lindegren et al. 2018). HD 63433 has $RUWE = 0.98$, consistent with the distribution of values seen for single stars. Based on a calibration of the companion parameter space that does induce excess noise, this corresponds to contrast limits of $\Delta G \sim 0$ mag at $\rho = 30$ mas, $\Delta G \sim 4$ mag at $\rho = 80$ mas, and $\Delta G \sim 5$ mag at $\rho \geq 200$ mas. The same evolutionary models would imply corresponding physical limits for equal-mass companions at $\rho \sim 0.7$ AU, $M < 0.4 M_\odot$ at $\rho \sim 1.8$ AU, and $M < 0.3 M_\odot$ at $\rho > 4.4$ AU.

Finally, the Gaia DR2 catalog (Lindegren et al. 2018) did not report any comoving, codistant companions within $< 1°$ of HD 63433. Oh et al. (2017) reported a co-moving companion based on Gaia DR1 astrometry, but the DR2 parameters for the two stars are inconsistent with each other and the claimed companion is $> 3°$ away from HD 63433. Given the Gaia catalog's completeness limit of $G \sim 20.5$ mag at moderately high galactic latitudes and sensitivity at $\rho > 3''$ (Ziegler et al. 2018; Brandeker & Cataldi 2019), the absence of wide companions corresponds to a physical limit of $M < 0.05 M_\odot$ at $\rho > 66$ AU to $\rho \sim 80,000$ AU.

4. LIGHT CURVE ANALYSIS

4.1. *Identification of the Transit Signals*

We identified a 7-day period planet candidate during a visual survey of the 2-minute cadence *TESS* Candidate Target List data (Stassun et al. 2018) via the light curve examining software LcTools[7] (Schmitt et al. 2019), which initially was introduced by Kipping et al. (2015). Further inspection revealed two additional transits of similar depth and duration located at 1844.057760 and 1864.606371 TBJD (BJD-2457000), indicating the presence of a second planet candidate with a period of approximately 21-days. The first candidate was released as a *TESS* object of interest (TOI) from analysis of the SPOC light curve, the first on Feb 19, 2020 and the second on Feb 20, 2020 (N. Guerrero et al. *submitted*), nearly simultaneous with our visual search. The SPOC data validation reports (Twicken et al. 2018; Li et al. 2019) note a significant centroid offset for the outer planet, but the offset is not consistent with any nearby source and such offsets are common for young variable stars (Newton et al. 2019). This offset was likely due to saturation (expected at $T = 6.27$) which degrades the centroids in the row direction.
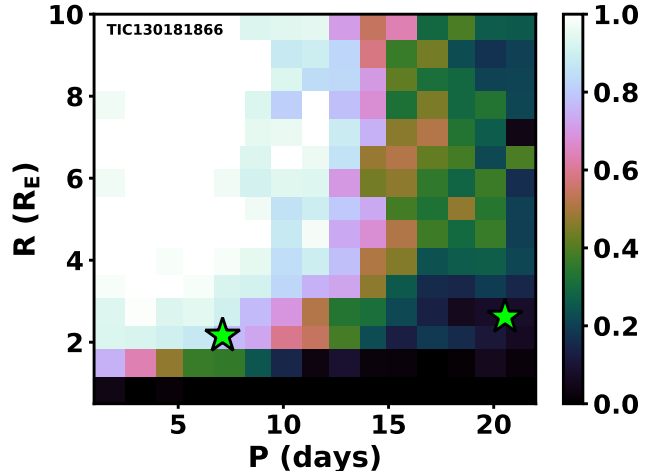
Figure 5. Completeness plot for the *TESS* light curve of HD 63433 based on the injection/recovery formalism described by Rizzuto et al. (2017). Regions are color-coded by the fraction of systems recovered. The two real planets are shown as green stars.

We searched for additional planets using the notch filter, as described in Rizzuto et al. (2017). We recovered the two planets identified above, but found no additional planet signals that passed all checks. Instead, we set limits on the existence of additional planets using an injection/recovery test, again following Rizzuto et al. (2017). To briefly summarize, we generated planets using the BATMAN package following a uniform distribution in period, b, and orbital phase. Half of the planet radii are drawn from a uniform distribution and the other half from a β distribution with coefficients $\alpha = 2$ and $\beta = 6$. We used this mixed distribution to ensure higher sampling around smaller and more common planets. We then detrended the light curve using the notch filter and searched for planets in the detrended curve using a Box-Least Squares (BLS) algorithm (Kovács et al. 2002). The results are summarized in Figure 5. We found that our search would be sensitive to $R_P \simeq 1 R_\oplus$ planets at periods of <5 d and $R_P \simeq 2 R_\oplus$ out to 15 d. We required at least two transits to consider a signal recovered, but the light curve covers <30 d, so most injected planets with > 15 d periods were not recovered.

4.2. *MCMC Fit of the Transit and HARPS-N Velocities*

We fit the *TESS* photometry simultaneously with the HARPS-N velocities during transit (of the RM effect) using the misttborn (MCMC Interface for Synthesis of Transits, Tomography, Binaries, and Others of a Rele-

vant Nature) fitting code[8] first described in Mann et al. (2016a) and expanded upon in Johnson et al. (2018). misttborn uses BATMAN (Kreidberg 2015) to generate model light curves and emcee (Foreman-Mackey et al. 2013) to explore the transit parameter space using an affine-invariant Markov chain Monte Carlo (MCMC) algorithm. We did not include any of the other radial velocities in this analysis, especially given the complication of stellar activity, as they are not precise enough to detect the reflex motion due to these small planets.

The standard implementation of misttborn fits for six parameters for each transiting planet: time of periastron (T_0), orbital period of the planet (P), planet-to-star radius ratio ($R_p/R_\star$), impact parameter (b), two parameters ($\sqrt{e}\sin\omega$ and $\sqrt{e}\cos\omega$) to characterize the orbital eccentricity (e) and argument of periastron (ω), as well as three parameters related to the star: the stellar density ($\rho_\star$) and the linear and quadratic limb-darkening coefficients (q_1, q_2) following the triangular sampling prescription of Kipping (2013).

To model stellar variations, misttborn includes a Gaussian Process (GP) regression module, utilizing the celerite code (Foreman-Mackey et al. 2017). For the GP kernel, we mostly followed Foreman-Mackey et al. (2017) and used a mixture of two stochastically driven damped simple harmonic oscillators (SHOs), at periods P_{GP} (primary) and $0.5P_{GP}$ (secondary). In addition to the stellar rotation period ($\ln(P_{GP})$), the light curve kernel is characterized by a variability amplitude of the fundamental signal ($\ln A_1$), the decay timescale for the secondary signal ($\ln Q_2$, the quality factor), the difference between the quality factor the first and second signal ($\ln\Delta Q = Q_1 - Q_2$), and a mix parameter (Mix) that describes the relative contribution of the two SHOs (where $A_1/A_2 = 1 + e^{-\mathrm{Mix}}$).

For the RM data, we used misttborn to fit for eight additional parameters for planet b. The primary parameters were the sky-projected spin-orbit misalignment (λ), the stellar rotation broadening ($v\sin i_*$), and the intrinsic width of the Gaussian line profile of individual surface elements (v_int), which approximates the combined effects of thermal, microturbulent, and macroturbulent broadening. We also included a quadratic polynomial fit to the out-of-transit variations in the radial velocity data (γ, $\dot\gamma$, and $\ddot\gamma$). We used a generic polynomial because the overall slope in the radial velocity curve is likely dominated by stellar activity, rather than a predictable sinusoidal curve induced by the planets. The last two parameters are the two limb-darkening co-

Table 5. Parameters and Priors

Parameter	Prior	
	planet b	planet c
T_0 (TJD)[a]	$\mathcal{U}[1916.4, 1916.5]$	$\mathcal{U}[1842, 1860]$
P (days)	$\mathcal{U}[0, 15]$	$\mathcal{U}[15, 30]$
$R_P/R_\star$	$\mathcal{U}[0, 1]$	$\mathcal{U}[0, 1]$
b	$\mathcal{U}[|b| < 1 + R_P/R_*]$	$\mathcal{U}[|b| < 1 + R_P/R_*]$
$\rho_\star$ ($\rho_\odot$)	$\mathcal{N}[1.30, 0.15]$	
$q_{1,1}$	$\mathcal{N}[0.30, 0.06]$	
$q_{2,1}$	$\mathcal{N}[0.37, 0.05]$	
$\sqrt{e}\sin\omega$	$\mathcal{U}[-1, 1]$	$\mathcal{U}[-1, 1]$
$\sqrt{e}\cos\omega$	$\mathcal{U}[-1, 1]$	$\mathcal{U}[-1, 1]$
$v\sin i_*$ (km s^{-1})	$\mathcal{N}[7.3, 0.3]$	...
λ (°)	$\mathcal{U}[-180, 180]$	...
$q_{1,\mathrm{RM}}$	$\mathcal{N}[0.53, 0.08]$	...
$q_{2,\mathrm{RM}}$	$\mathcal{N}[0.39, 0.06]$	...
v_int (km s^{-1})	$\mathcal{N}[4.2\ 1.2]$	...
γ_1 (km s^{-1})	$\mathcal{U}[-17, -14]$	...
$\dot\gamma$ (km s^{-1})	$\mathcal{U}[-1, 1]$	...
$\ddot\gamma$ (km s^{-1})	$\mathcal{U}[-1, 1]$	...
$\ln P_{GP}$	$\mathcal{U}[1, 2]$	
$\ln A_1$	$\mathcal{U}[-\infty, 1]$	
$\ln(Q_0)$	$\mathcal{U}[0.5, \infty]$	
$\ln\Delta Q$	$\mathcal{U}[0, \infty]$	
Mix	$\mathcal{U}[-10, 10]$	

NOTE—$\mathcal{U}[X, Y]$ denotes a uniform prior limited to between X and Y and $\mathcal{N}[X, Y]$ a Gaussian prior with mean X and standard deviation Y.

[a] It is standard to report T_0 as the mid-transit point for the *first* transit. However, for computational reasons in the RM fit, we restrict T_0 around the RM observations for planet b.

efficients ($q_{1,\mathrm{RM}}$ and $q_{2,\mathrm{RM}}$). These RM limb-darkening parameters were fit separately from those for the photometry because of differences in the HARPS-N and *TESS* wavelength coverage. From these parameters, we produced an analytic RM model following the methodology of Hirano et al. (2011) and Addison et al. (2013). This model consists of an analytic function of $v\sin i$ and v_int, multiplied by the flux drop due to the transiting planet; we calculated the flux decrement needed for this model with BATMAN, following the same methodology as for the photometric light curves. We note that the GP described above is not used for the RM data, only the photometric curve. '

We ran two separate MCMC chains, the first as described above, and the second with e and ω locked at 0. For both chains, we ran the MCMC using 100 walkers for 250,000 steps including a burn-in of 20,000 steps. The autocorrelation time indicated that this was sufficient for convergence. We also applied Gaussian priors on the limb-darkening coefficients (both for *TESS* and the HARPS-N data) based on the values in Claret & Bloemen (2011) and Parviainen & Aigrain (2015), with

errors accounting for the difference between these two estimates (which differ by 0.05-0.07). For $v \sin i_*$ and $v_{\rm int}$, we used Gaussian priors of $7.3 \pm 0.3 \, {\rm km \, s^{-1}}$ and $4.2 \pm 1.2 \, {\rm km \, s^{-1}}$ based on analysis from Section 3.5 and the investigation of Doyle et al. (2014). For the fit with $e = 0$, we applied Gaussian priors for the stellar density taken from our derived stellar parameters derived in Section 3.2. All other parameters were sampled uniformly with physically motivated boundaries: $\sqrt{e} \sin \omega$ and $\sqrt{e} \cos \omega$ were restricted to $(-1, 1)$, $|b| < 1 + R_p/R_s$, and T_0 to the time period sampled by the data. The GP mix parameter was restricted to be between -10 and 10. We let the linear and quadratic terms of the radial velocity curve in the RM data float, as this is produced by some combination of actual reflex motion of the star due to the two planets, and stellar activity of this young, relatively rapidly rotating star. The full list of fit parameters, priors, and imposed limits are given in Table 5.

The resulting fit light curve is shown in Figure 6 with the velocity curve in Figure 7. The best fitting model and derived parameters, along with 68% credible intervals are listed in Table 6. Figures 8a and b show partial posteriors for the MCMC-fit parameters[9].

The GP fit accurately reproduced the overall out-of-transit variability (Figure 6). Similarly, the resulting period matched the rotation period from Section 3.1 (6.54 d versus 6.45 d), and agrees with the predicted value for the star's mass and membership to UMaG (6.9 ± 0.4 d).

The transit duration suggests a low eccentricity for both planets ($e < 0.2$), as is common for multi-transiting systems (Van Eylen & Albrecht 2015). Our analysis did not include any correction for biases in the eccentricity distribution of planets (Kipping 2014), but accounting for this would only drive the resulting eccentricity values down. Consistent with this, the ρ_* derived from the transit assuming $e = 0$ and a uniform density prior yields $\rho_* = 1.331^{+0.056}_{-0.1} \rho_\odot$, in excellent agreement with our derived value from Section 3 ($\rho_* = 1.3 \pm 0.15 \rho_\odot$). Thus, if we were to assume that the eccentricities are $\simeq 0$, we can consider this an additional verification of our adopted stellar parameters.

Due to the relatively low amplitude of the RM effect for HD 63433 b and the complication of stellar activity, our posterior for the sky-projected spin-orbit misalignment λ is broad. However, we clearly demonstrated that the planetary orbit is prograde; retrograde orbits would yield $|\lambda| > 90°$, which is completely ruled out (Figure 8).

---

[9] Trimmed posteriors for all parameters are available at https://github.com/awmann/THYME3_HD63433

We discuss the implications of this measurement in more detail in Section 7. Furthermore, we clearly detected the RM effect due to the transit of HD 63433 b (the signal is inconsistent with no RM signal), confirming that the planet is real.

As an additional test on our RM fit, we ran an MCMC chain using a linear trend in velocity rather than a second-order polynomial (i.e., $\ddot{\gamma}$ fixed at 0). The resulting λ posterior was not significantly different ($\lambda = 7.0 \pm 35°$). The second-order polynomial was preferred statistically ($\Delta BIC = 5$), so we use it for all results reported in Table 6.

5. FALSE-POSITIVE ANALYSIS

While planet b was confirmed through detection of the RM signal, we have no such detection for planet c. We instead validated the planet statistically by considering the three false-positive scenarios below.

5.1. *Eclipsing Binary*

We compared the wealth of radial velocity data (Table 1) to the predicted velocity curve of a planet or binary at the orbital period of the outer planet (20.5 d). We assumed a low eccentricity ($e < 0.1$) and sampled over the whole range of ω and mass ratios. We included a zero-point correction term between instruments, which takes the value preferred by the predicted/model velocity curve. Including this term meant that 2-3 epochs each from TRES and NRES provided little information, and were not included. To account for stellar jitter and instrumental drift, we inflated errors in the velocities based on the scatter between points for each instrument ($37 \, {\rm m \, s^{-1}}$ for SOPHIE/ELODIE and $24 \, {\rm m \, s^{-1}}$ for Lick).

The velocities are not precise enough to detect either planet, but easily rules out (at 99.7%) any stellar or planetary companion down to $\simeq$Jupiter-mass at the orbital period of planet c (Figure 9).

5.2. *Background Eclipsing Binary*

As detailed in Vanderburg et al. (2019), if the observed transits are due to blends from a background eclipsing/transiting system, the true radius ratio can be determined from the ratio of the ingress time (T_{12} or T_{34}) to the time between first and third contact (T_{13}). This provides a constraint on the brightest possible background source that could produce the observed transit depth: $\Delta m_{\rm TESS} \leq 2.5 \log_{10}(T_{12}^2/T_{13}^2/\delta)$, where δ is the transit depth. Using our results from Section 4, we find $\Delta m < 2.4$ mag at 99.7% confidence. The combination of AO imaging and *G*aia DR2 (Section 3.6) rule out any such background star down to <80 mas and out to $4.5'$.

We also rule out a background eclipsing binary behind HD 63433. The high-resolution imaging spans 9
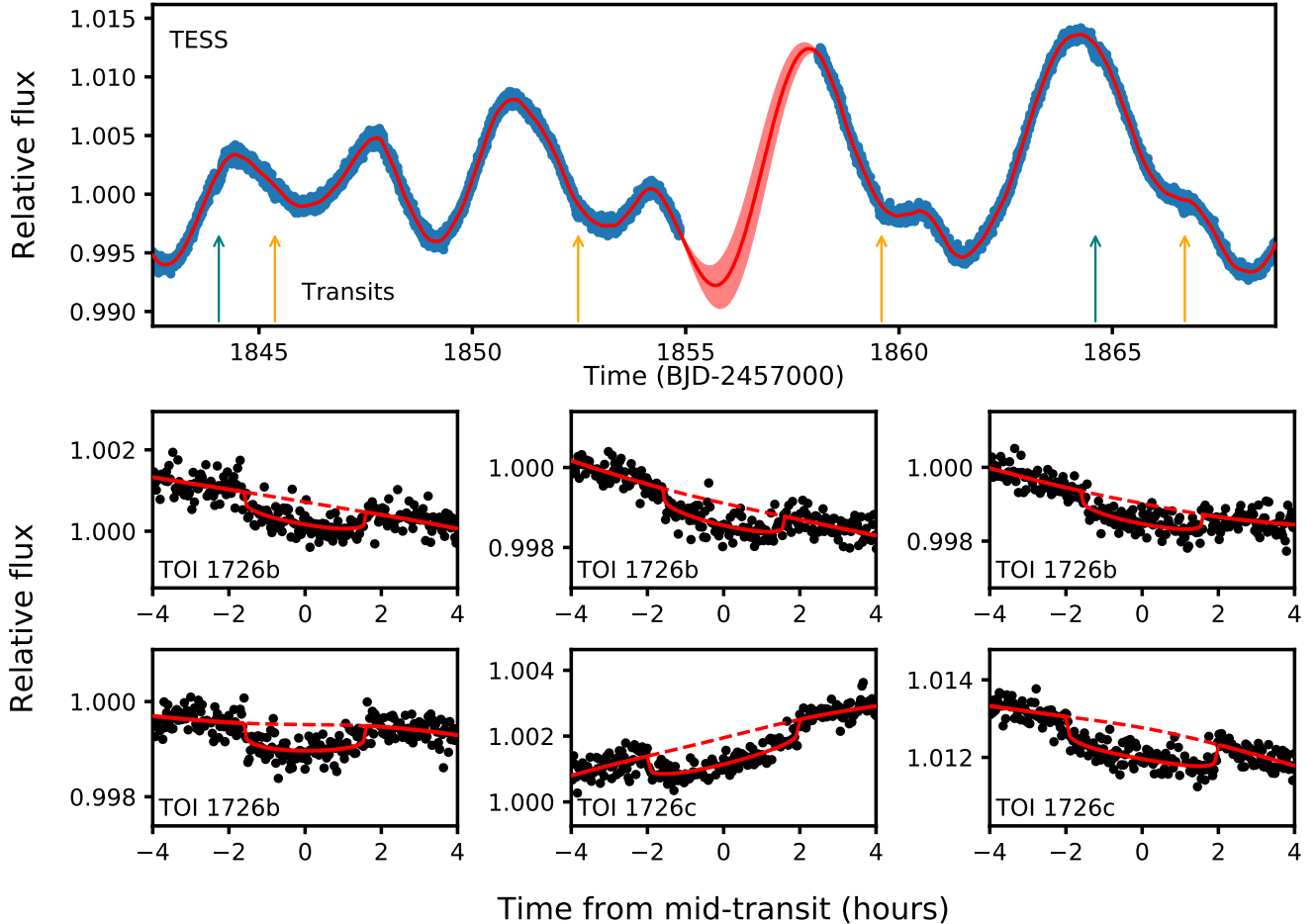
Figure 6. *TESS* light curve of HD 63433. The top panel shows the PDCSAP curve (blue) after filtering out outliers, as well as our best-fit GP model (red). The locations of the transits are shown with arrows along the x-axis, red for planet b and teal for c. The bottom set of six panels shows the six individual transit events centered on the mid-transit time with the best-fit model (red solid) and the best-fit model for the out-of-transit variability only (the GP; red dashed). Note that the x-axis scale and range of all individual transits are the same (hours from mid-transit), but differ from the top panel (days), and y-axis ranges vary.

years (1999.16–2008.28) and is sensitive to companions brighter than our magnitude threshold down to 80 mas. Due to its proper motion, HD 63433 has moved more than 100 mas over the same time period; thus, any foreground or background star not visible in the earliest dataset would be visible in the final observation.

5.3. *Companion Eclipsing Binary*

To explore the range of possible stellar companions, we used a Monte Carlo simulation of 5×10^6 binaries, comparing each generated system to the velocities, high-resolution imaging, and limits from *G*aia imaging and astrometry. Companions were generated following a log-normal distribution in period following (Raghavan et al. 2010), but uniform in other orbital parameters. The radial velocity data listed in Table 1 span more than 22 years, which overlaps in parameter space with the

high-contrast imaging data (down to $\simeq 1\,\mathrm{AU}$) and *G*aia constraints. A negligible fraction ($< 0.01\%$) of generated companions are consistent with the external constraints, resolved in *TESS*, and reproduce the observed transit depth, statistically ruling out this scenario.

6. DYNAMICAL ANALYSIS

Studying the dynamical state of exoplanetary systems provides insights into the interations between planets, their orbital evolution, and the possibility of additional, undetected planets in the system (e.g., Li et al. 2014; Kane & Blunt 2019). The latter of these is particularly important for compact planetary systems, which are commonly dynamically filled (Fang & Margot 2013). To investigate these effects, we used the Mercury Integrator Package (Chambers 1999) to conduct N-body integrations of the system. For this analysis, we adopt the
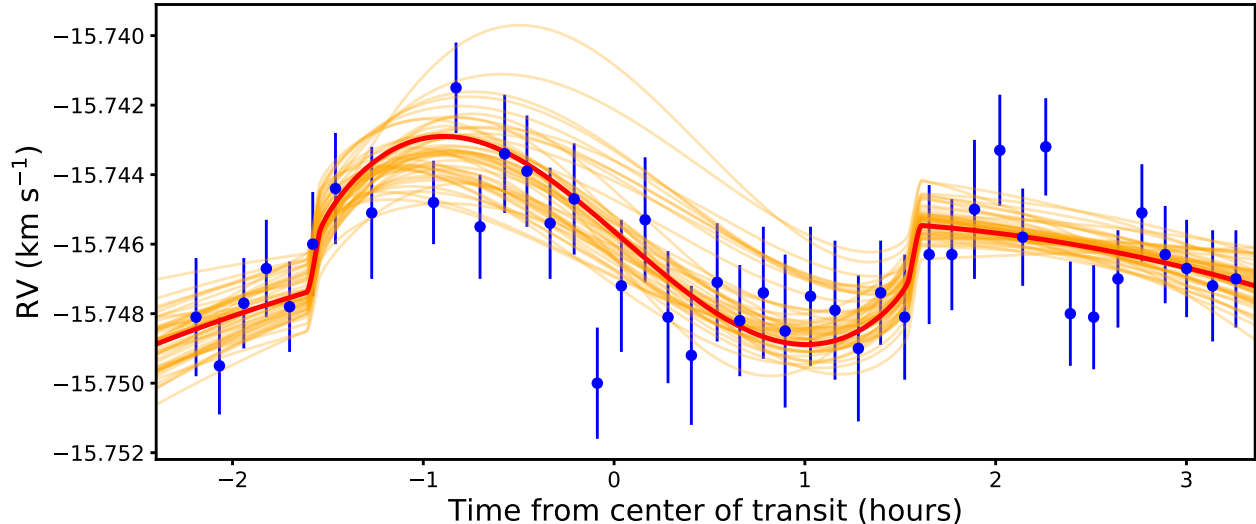
Figure 7. HARPS-N velocities and errors (blue points) compared to our best-fit RM model (red) and 50 random solutions drawn from the MCMC posteriors (orange). The orbit is clearly prograde, and the data favors a low value of λ (larger amplitude), but a wide range of λ values are allowed by the data.

stellar properties provided by Table 3 and the planetary properties (for the e, ω float case) provided by Table 6. We used the methodology described by Kane (2015, 2019), which both explores the intrinsic dynamical stability of the system using the observed parameters, and inserts additional planets to test the viability of possible additional planets. The time step of the integrations was set to 0.2 days in order to adequately sample the orbital period of the inner planet (Duncan et al. 1998). Since only the planetary radii are provided by the measurements described in this work, we estimate the planetary masses using the probabilistic forecasting method of Chen & Kipping (2017). For both planet b and c, these masses are computed as 5.5 and 7.3 $M_\oplus$ respectively. We then executed an initial single dynamical simulation for 10^7 simulation years that demonstrated the observed orbital architecture is a stable configuration. The chosen time step of 0.2 days maintained an energy conservation error of $dE/E \sim 10^{-9}$. To test for further stable locations, we inserted an Earth-mass planet at locations within the range 0.05–0.18 AU, which encompasses the semi-major axes of both planets (see Table 6). This process sampled several hundred locations within that range with the simulated planet placed at random starting locations. The results of this suite of simulations revealed that there is a stable island where an additional Earth-mass planet could be harbored located in the semi-major axis range of 0.099-0.112 AU. Even if present and transiting, such a planet is below the detection sensitivity of the photometry (Figure 5). To fully explore the range of allowable planetary masses between planets b and c, we

repeated the above analysis with an inserted Neptune, Saturn, and Jupiter-mass planet. The stable island between the planets were largely retained for the Neptune and Saturn-mass injected planets, but completely disappeared for the Jupiter-mass case. Thus Jupiter-mass planets are dynamically ruled out between the b and c planets, and transits of a Saturn-mass (Jupiter-radius) planet are ruled out by the photometry, but could still be present in a non-transiting capacity.

7. SUMMARY & DISCUSSION

We presented the discovery, characterization, and confirmation/validation of two planets transiting the bright ($V = 6.9$ mag; Figure 10) star HD 63433, a Sun-like star ($M_* = 0.99 \pm 0.03 M_\odot$). Based on its kinematics, lithium abundance, and rotation, we confirmed HD 63433 to be a member of the 414 Myr old Ursa Major Moving Group. In addition to membership, we updated the stellar properties of HD 63433 based on the SED, *Gaia* DR2 distance, and existing high-resolution spectroscopy. Using the *TESS* light curve, we determined the two planets have radii of $2.15 \pm 0.10 R_\oplus$ and $2.67 \pm 0.12 R_\oplus$ and periods of 7.11 d and 20.54 d, respectively. We simultaneously fit the *TESS* light curve with the HARPS-N spectroscopy of the RM effect taken during a transit of the inner planet. In addition to confirming the planet, the HARPS-N data demonstrate that the planet has a prograde orbit. Lastly, we validated the outer planet by ruling out non-planetary explanations for the observed signal.

Table 6. Transit-Fit Parameters.

Parameter	Planet b	Planet c	Planet b	Planet c
	e,ω fixed		e,ω free	
Transit Fit Parameters				
T_0 (TJD)	$1916.4526^{+0.0032}_{-0.0027}$	$1844.05799^{+0.00084}_{-0.00087}$	$1916.4533^{+0.0037}_{-0.0027}$	$1844.05791^{+0.0008}_{-0.00076}$
P (days)	$7.10793^{+0.0004}_{-0.00034}$	$20.5453^{+0.0012}_{-0.0013}$	$7.10801^{+0.00046}_{-0.00034}$	20.5455 ± 0.0011
$R_P/R_\star$	0.02161 ± 0.00055	0.02687 ± 0.0007	$0.02168^{+0.00065}_{-0.00058}$	$0.02637^{+0.00077}_{-0.00074}$
b	$0.18^{+0.17}_{-0.13}$	$0.512^{+0.063}_{-0.033}$	$0.26^{+0.19}_{-0.17}$	$0.29^{+0.21}_{-0.2}$
$\rho_\star$ ($\rho_\odot$)	$1.293^{+0.079}_{-0.2}$		1.3 ± 0.14	
$q_{1,1}$	$0.302^{+0.058}_{-0.057}$		$0.299^{+0.06}_{-0.055}$	
$q_{2,1}$	0.369 ± 0.048		0.372 ± 0.048	
$\sqrt{e}\sin\omega$	0 (fixed)	0 (fixed)	$-0.08^{+0.11}_{-0.13}$	$0.09^{+0.13}_{-0.18}$
$\sqrt{e}\cos\omega$	0 (fixed)	0 (fixed)	$0.01^{+0.35}_{-0.37}$	$0.09^{+0.39}_{-0.43}$
Rossiter-McLaughlin Parameters				
$v\sin i_\star$ (km s^{-1})	7.28 ± 0.29	$\cdots$	$7.3^{+0.29}_{-0.3}$	$\cdots$
λ (°)	$1.0^{+41.0}_{-43.0}$	0 (fixed)	$8.0^{+33.0}_{-45.0}$	0 (fixed)
$q_{1,\mathrm{RM}}$	$0.534^{+0.08}_{-0.081}$		$0.524^{+0.084}_{-0.078}$	
$q_{2,\mathrm{RM}}$	$0.388^{+0.056}_{-0.059}$		$0.388^{+0.057}_{-0.059}$	
v_{int} (km s^{-1})	4.3 ± 1.1	$\cdots$	4.2 ± 1.2	$\cdots$
γ_1 (km s^{-1})	$-15.74559^{+0.0007}_{-0.00064}$	$\cdots$	$-15.74542^{+0.00075}_{-0.0007}$	$\cdots$
$\dot{\gamma}$ (km s^{-1} day^{-1})	$0.0144^{+0.0049}_{-0.0048}$	$\cdots$	$0.014^{+0.0048}_{-0.0049}$	$\cdots$
$\ddot{\gamma}$ (km s^{-1} day^{-2})	-0.184 ± 0.078	$\cdots$	$-0.198^{+0.082}_{-0.083}$	$\cdots$
Gaussian Process Parameters				
$\log(P_{GP})$	\multicolumn{2}{c}{$1.872^{+0.018}_{-0.017}$}		\multicolumn{2}{c}{1.872 ± 0.017}	
$\log(A_1)$	\multicolumn{2}{c}{$-8.5^{+1.7}_{-1.2}$}		\multicolumn{2}{c}{$-8.6^{+1.6}_{-1.1}$}	
$\log(\Delta Q)$	\multicolumn{2}{c}{$1.6^{+1.9}_{-1.1}$}		\multicolumn{2}{c}{$1.6^{+1.9}_{-1.2}$}	
$\log(Q_0)$	\multicolumn{2}{c}{$3.07^{+1.42}_{-0.85}$}		\multicolumn{2}{c}{$3.03^{+1.3}_{-0.82}$}	
Mix	\multicolumn{2}{c}{$-3.5^{+1.3}_{-1.9}$}		\multicolumn{2}{c}{$-3.3^{+1.3}_{-1.9}$}	
Derived Parameters				
$a/R_\star$	$16.95^{+0.34}_{-0.82}$	$34.38^{+0.69}_{-2.0}$	$16.75^{+0.47}_{-0.74}$	$36.1^{+1.1}_{-1.7}$
i (°)	$89.38^{+0.43}_{-0.64}$	$89.147^{+0.069}_{-0.2}$	$89.1^{+0.59}_{-0.69}$	$89.51^{+0.34}_{-0.35}$
δ (%)	$0.0467^{+0.0024}_{-0.0023}$	$0.0722^{+0.0038}_{-0.0037}$	$0.047^{+0.0029}_{-0.0025}$	$0.0696^{+0.0041}_{-0.0038}$
T_{14} (days)	$0.134^{+0.0014}_{-0.0013}$	$0.1695^{+0.0015}_{-0.0013}$	$0.133^{+0.018}_{-0.02}$	0.17 ± 0.031
T_{23} (days)	$0.1279^{+0.0013}_{-0.0012}$	$0.1573^{+0.0014}_{-0.0015}$	$0.127^{+0.016}_{-0.02}$	0.159 ± 0.029
$g_{1,1}$	$0.402^{+0.063}_{-0.06}$		$0.403^{+0.062}_{-0.059}$	
$g_{2,1}$	$0.143^{+0.058}_{-0.054}$		$0.139^{+0.058}_{-0.054}$	
$g_{1,\mathrm{RM}}$	$0.562^{+0.094}_{-0.093}$		$0.558^{+0.091}_{-0.094}$	
$g_{2,\mathrm{RM}}$	$0.162^{+0.088}_{-0.081}$		$0.161^{+0.087}_{-0.082}$	
e	0 (fixed)	0 (fixed)	$0.085^{+0.179}_{-0.067}$	$0.114^{+0.204}_{-0.068}$
R_p ($R_\oplus$)[b]	2.15 ± 0.10	2.67 ± 0.12	2.15 ± 0.10	2.64 ± 0.12
a (AU)[a]	$0.0719^{+0.0031}_{-0.0044}$	$0.1458^{+0.0062}_{-0.0101}$	$0.0710^{+0.0033}_{-0.0041}$	$0.1531^{+0.0074}_{-0.0092}$

[a] R_p derived using the $R_\star$ value from Table 3

The two planets around HD 63433 add to the growing number of known transiting planets around young stars that are members of young (<1 Gyr) clusters or moving groups (Rizzuto et al. 2017; Curtis et al. 2018). As the sample grows, it will enable studies into the evolution of planetary systems through the statistical comparison of young and old planetary systems, which in turn yields information about how exoplanets evolve.

HD 63433 b is the second young small planet with a published measurement of its spin-orbit alignment, after DS Tuc b (Zhou et al. 2020; Montet et al. 2020), and the first in a multiplanet system. Both DS Tuc b

and HD 63433 b show prograde orbits. However, with the data currently in hand, our constraints on the spin-orbit alignment are poor. Further RM observations of multiple transits to increase the overall signal-to-noise and average over the effects of stellar activity will allow us to measure λ more precisely. Nonetheless, HD 63433 is consistent with the trend of aligned orbits for compact multiplanet systems (Albrecht et al. 2013; Zhou et al. 2018), with only a few exceptions (Huber et al. 2013; Dalal et al. 2019).

We found in Section 3.5 that the stellar rotation axis is likely to lie approximately in the plane of the sky.
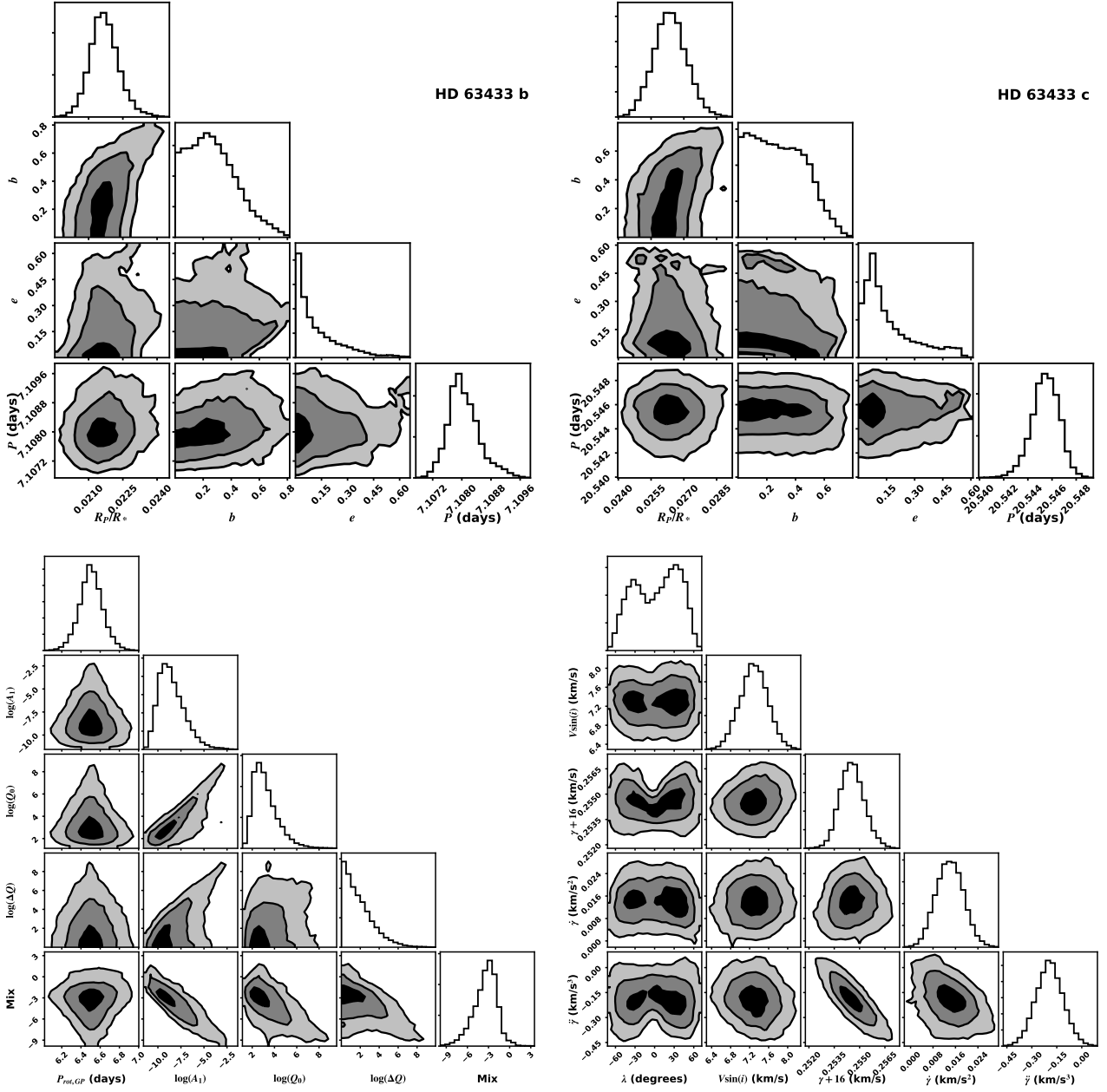
Figure 8. Posterior density and correlations for a subset of the parameters for planet b (top left), planet c (top right), the GP modelling (bottom left) and the RM fit (bottom right). A small percentage ($< 1\%$) of points are cut off the plot edges for clarity. All parameters are fit simultaneously, but are shown as separate panels for clarity. We show physical parameters here rather than fitted ones, e.g., MCMC explores $\sqrt{e}\cos(\omega)$ and $\sqrt{e}\sin(\omega)$ while e is shown here. See Section 4 for more details.
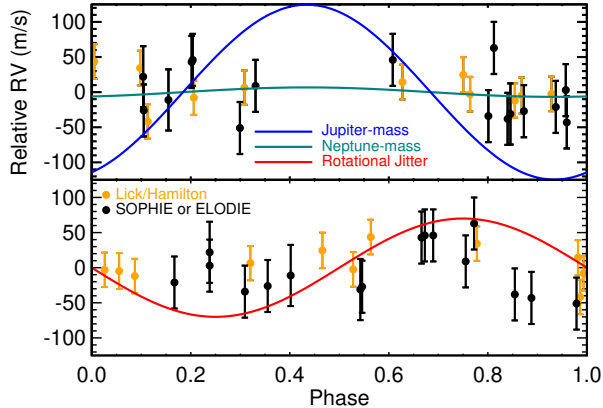
Figure 9. Top: velocities from Lick/Hamilton (orange) and SOPHIE or ELODIE (black) compared to the expected curve for a Jupiter- (blue) or Neptune-mass (teal) planet matching the orbital period of planet c. Bottom: the same velocities folded to the rotation period of the star and the approximate rotational jitter (red) expected from the *TESS* light curve and $v \sin i_*$. Measurement have been inflated from their reported values based on the scatter between points.

Taken together with the sky-projected spin-orbit misalignment, this suggests that the planets are aligned in 3D. Indeed, using Eqn. 7 of Winn et al. (2007) and our measured values of the stellar and planetary inclinations and the spin-orbit misalignment, we calculate a 3-dimensional spin-orbit misalignment of $\psi < 50°$ at 1σ confidence. A more precise future measurement of λ would also allow better constraints on ψ, as this is currently the limiting factor on the precision of ψ.

7.1. *Prospects for Follow-up*

Thanks to HD 63433's brightness ($V = 6.9$, $K = 5.3$; see Figure 10), this system is ideal for a variety of follow-up observations to characterize the planets and the system as a whole. Observations over the coming years will allow us to determine the system's 3-D architecture, measure mass loss from the planets and study their atmospheres, and potentially measure the masses of the planets.

The HARPS-N observations of the b transit demonstrate that HD 63433 is well-suited for additional RM observations. Repeat observations of the planet b would enable more detailed accounting of stellar variability (Zhou et al. 2020; Montet et al. 2020) and provide more robust constraints on λ. Observations of the c transit would both confirm the planet and allow a measurement of the mutual inclination between the orbits of the two planets.

One of the first discoveries from the young planet population has been that young planets are statisti-

cally larger than their older counterparts (e.g., Rizzuto et al. 2018; Mann et al. 2018). This offset could be explained by thermal contraction of an H/He dominated atmosphere (Lopez & Fortney 2014), atmospheric mass-loss from interactions with the (still-active) host-star (Murray-Clay et al. 2009), or photochemical hazes making the atmosphere larger and puffier (Gao & Zhang 2020). Right now, the difference is only an offset in the planet radius distribution with age, making it difficult to distinguish between these scenarios. Instead, planet masses (and hence densities) are needed. While challenging, both of HD 63433's planets may be within reach of existing PRV spectrographs. Assuming masses of $5.5 M_\oplus$ and $7.3 M_\oplus$ for planets b and c respectively (Chen & Kipping 2017), the predicted radial-velocity amplitudes are $\simeq 2\,\mathrm{m\,s^{-1}}$. This signal is within the reach of existing instruments, but still much smaller than the estimated stellar jitter ($20–30\,\mathrm{m\,s^{-1}}$; Figure 9 and Table 1). The planet b is especially challenging given the similarity of its orbital period to the stellar rotation period (7.11 d versus 6.45 d). However, a focused campaign designed to separate planetary and stellar signals, as was done for the young system K2-100 (Barragán et al. 2019), will likely yield a mass constraint for planet c.

Wang & Dai (2019) and Gao & Zhang (2020) argue that young planets are likely to have flat transmission spectra due to either dust or photochemical hazes. There is some evidence to support this from transmission spectroscopy follow-up of young systems (Libby-Roberts et al. 2020; Thao et al. 2020). However, a wider set of observations are required to explore under what conditions young atmospheres are dominated by hazes, dust, and/or clouds. Because the host is bright ($H \simeq 5$), both planets are well within reach of transmission spectroscopy with *HST* or *JWST*.

Both of the planets lie on the large-radius, gas-rich side of the radius valley (e.g., Owen & Wu 2013; Fulton & Petigura 2018). Given the young age of the system, it is likely that both planets are actively losing their atmospheres through photoevaporation (e.g. Owen & Jackson 2012; Lopez & Fortney 2013) or core-powered mass-loss (Ginzburg et al. 2018). Given the X-ray flux of HD 63433 observed by XMM-Newton as a part of its slew catalog (94 erg s^{-1} cm^2) and the energy-limited mass-loss relation (e.g. Owen 2019), we estimate mass-loss rates of $\eta \approx 2.79 \times 10^{11}$ g s^{-1} and $\eta \approx 7.07 \times 10^{10}$ g s^{-1} for b and c, respectively, where η describes the heating efficiency of the atmospheres. This is higher than many other planets of similar size, including Gl 436b and GJ 3470b, both of which have detected exospheres (Ehrenreich et al. 2015; Ninan et al. 2020).
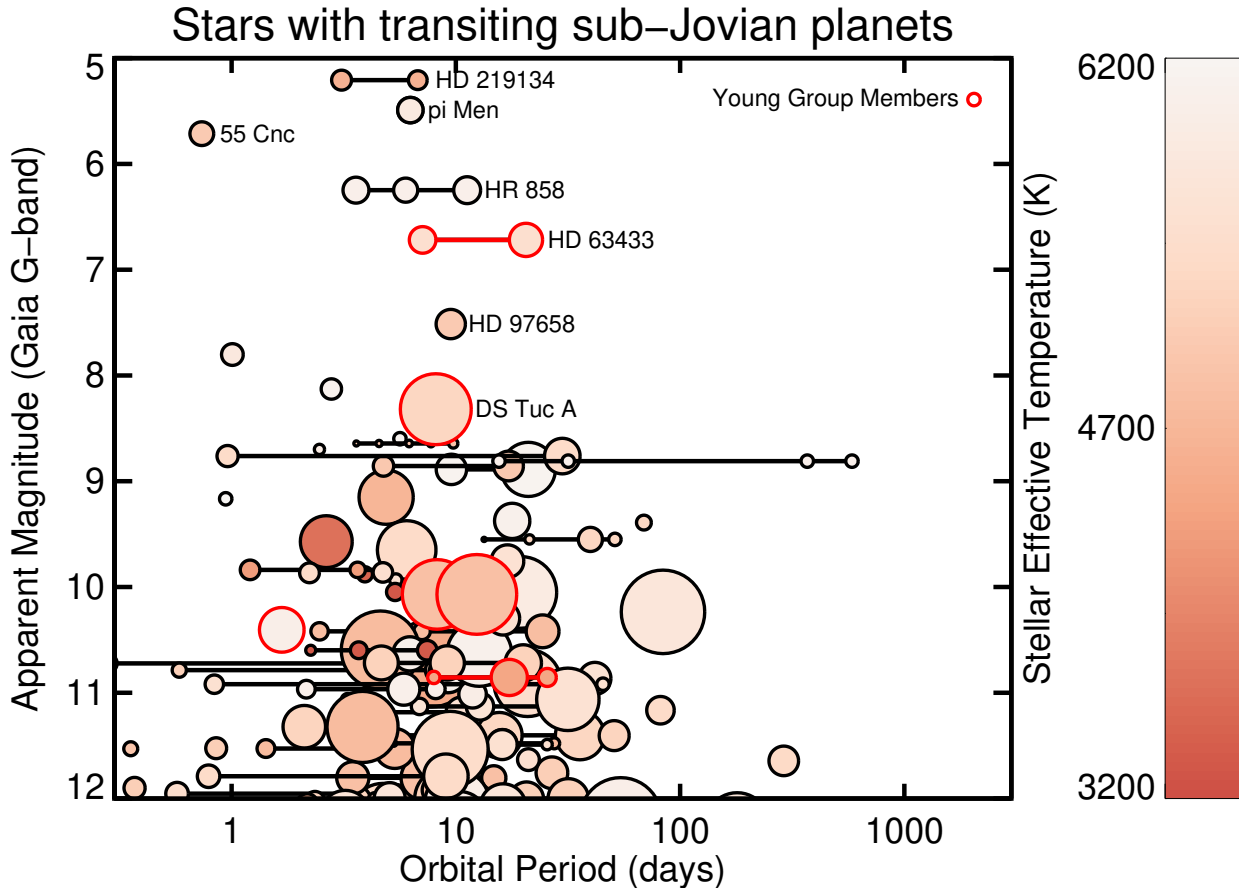
Figure 10. HD 63433 in context with the population of known small ($R_p < 7\ R_\oplus$) transiting planets, in terms of orbital period and host star brightness. Symbol size is proportional to the planetary radius, and symbol color to stellar effective temperature; planets transiting the same star are connected by lines, and non-transiting planets in these systems are not depicted. Several of the brightest systems are labeled; those in bold are *TESS* discoveries, while those in normal type were previous discoveries. We highlight planets in young (< 1 Gyr) clusters and associations in red. HD 63433 is among the brightest stars known to host transiting planets, and is a prime target for a variety of follow-up observations.

Facilities: TESS, WWVSH 0.6m, LCOGT 1m (Sinistro), LCOGT 1m (NRES), SMARTS 1.5m (CHIRON), Tillinghast 1.5m (TRES), SOAR (Goodman), TNG (HARPS-N), OHP 1.93m (ELODIE), OHP 1.93m (SOPHIE), Shane 3m (Hamilton), . . .

Software: LcTools, misttborn.py, *emcee* (Foreman-Mackey et al. 2013), *batman* (Kreidberg 2015), matplotlib (Hunter 2007), corner.py (Foreman-Mackey 2016), AstroImageJ (Collins et al. 2017), BANZAI (McCully et al. 2018)

REFERENCES

Addison, B. C., Tinney, C. G., Wright, D. J., et al. 2013, ApJL, 774, L9, doi: 10.1088/2041-8205/774/1/L9

Aguilera-Gómez, C., Ramírez, I., & Chanamé, J. 2018, A&A, 614, A55, doi: 10.1051/0004-6361/201732209

Albrecht, S., Winn, J. N., Marcy, G. W., et al. 2013, ApJ, 771, 11, doi: 10.1088/0004-637X/771/1/11

Allard, F., Homeier, D., & Freytag, B. 2011, in Astronomical Society of the Pacific Conference Series, Vol. 448, 16th Cambridge Workshop on Cool Stars, Stellar Systems, and the Sun, ed. C. Johns-Krull, M. K. Browning, & A. A. West, 91. https://arxiv.org/abs/1011.5405

Ammler-von Eiff, M., Bedalov, A., Kranhold, C., et al. 2016, A&A, 591, A84, doi: 10.1051/0004-6361/201526625

Ammler-von Eiff, M., & Guenther, E. W. 2009, A&A, 508, 677, doi: 10.1051/0004-6361/200912660

Angus, R., Aigrain, S., Foreman-Mackey, D., & McQuillan, A. 2015, MNRAS, 450, 1787, doi: 10.1093/mnras/stv423

Baraffe, I., Homeier, D., Allard, F., & Chabrier, G. 2015, A&A, 577, A42, doi: 10.1051/0004-6361/201425481

Baranne, A., Queloz, D., Mayor, M., et al. 1996, A&AS, 119, 373

Barragán, O., Aigrain, S., Kubyshkina, D., et al. 2019, MNRAS, 490, 698, doi: 10.1093/mnras/stz2569

Baumann, P., Ramírez, I., Meléndez, J., Asplund, M., & Lind, K. 2010, A&A, 519, A87, doi: 10.1051/0004-6361/201015137

Benatti, S., Nardiello, D., Malavolta, L., et al. 2019, A&A, 630, A81, doi: 10.1051/0004-6361/201935598

Blackwell, D. E., & Shallis, M. J. 1977, MNRAS, 180, 177

Boesgaard, A. M., Lum, M. G., Deliyannis, C. P., et al. 2016, ApJ, 830, 49, doi: 10.3847/0004-637X/830/1/49

Boisse, I., Pepe, F., Perrier, C., et al. 2012, A&A, 545, A55, doi: 10.1051/0004-6361/201118419

Bouchy, F., Díaz, R. F., Hébrard, G., et al. 2013, A&A, 549, A49, doi: 10.1051/0004-6361/201219979

Bouvier, J., Barrado, D., Moraux, E., et al. 2018, A&A, 613, A63, doi: 10.1051/0004-6361/201731881

Brandeker, A., & Cataldi, G. 2019, A&A, 621, A86, doi: 10.1051/0004-6361/201834321

Brandt, T. D., & Huang, C. X. 2015, ApJ, 807, 58, doi: 10.1088/0004-637X/807/1/58

Brown, T. M., Baliber, N., Bianco, F. B., et al. 2013, PASP, 125, 1031, doi: 10.1086/673168

Buchhave, L. A., Bakos, G. Á., Hartman, J. D., et al. 2010, ApJ, 720, 1118, doi: 10.1088/0004-637X/720/2/1118

Buchhave, L. A., Latham, D. W., Johansen, A., et al. 2012, Nature, 486, 375, doi: 10.1038/nature11121

Chambers, J. E. 1999, MNRAS, 304, 793, doi: 10.1046/j.1365-8711.1999.02379.x

Chen, J., & Kipping, D. 2017, ApJ, 834, 17, doi: 10.3847/1538-4357/834/1/17

Choi, J., Dotter, A., Conroy, C., et al. 2016, ApJ, 823, 102, doi: 10.3847/0004-637X/823/2/102

Christiansen, J. L., Crossfield, I. J. M., Barentsen, G., et al. 2018, AJ, 155, 57, doi: 10.3847/1538-3881/aa9be0

Cieza, L. A., Cochran, W. D., & Augereau, J.-C. 2008, ApJ, 679, 720, doi: 10.1086/586887

Claret, A., & Bloemen, S. 2011, A&A, 529, A75, doi: 10.1051/0004-6361/201116451

Clemens, J. C., Crain, J. A., & Anderson, R. 2004, in Proc. SPIE, Vol. 5492, Ground-based Instrumentation for Astronomy, ed. A. F. M. Moorwood & M. Iye, 331–340, doi: 10.1117/12.550069

Collins, K. A., Kielkopf, J. F., Stassun, K. G., & Hessman, F. V. 2017, AJ, 153, 77, doi: 10.3847/1538-3881/153/2/77

Cosentino, R., Lovis, C., Pepe, F., et al. 2012, in Society of Photo-Optical Instrumentation Engineers (SPIE) Conference Series, Vol. 8446, Proc. SPIE, 84461V, doi: 10.1117/12.925738

Cosentino, R., Lovis, C., Pepe, F., et al. 2014, in Society of Photo-Optical Instrumentation Engineers (SPIE) Conference Series, Vol. 9147, Proc. SPIE, 91478C, doi: 10.1117/12.2055813

Courcol, B., Bouchy, F., Pepe, F., et al. 2015, A&A, 581, A38, doi: 10.1051/0004-6361/201526329

Curtis, J. L., Vanderburg, A., Torres, G., et al. 2018, AJ, 155, 173, doi: 10.3847/1538-3881/aab49c

Cushing, M. C., Marley, M. S., Saumon, D., et al. 2008, ApJ, 678, 1372, doi: 10.1086/526489

Cutri, R. M., & et al. 2014, VizieR Online Data Catalog, II/328

Dahm, S. E. 2015, ApJ, 813, 108, doi: 10.1088/0004-637X/813/2/108

Dalal, S., Hébrard, G., Lecavelier des Étangs, A., et al. 2019, A&A, 631, A28, doi: 10.1051/0004-6361/201935944

David, T. J., & Hillenbrand, L. A. 2015, ApJ, 804, 146, doi: 10.1088/0004-637X/804/2/146

David, T. J., Petigura, E. A., Luger, R., et al. 2019, ApJL, 885, L12, doi: 10.3847/2041-8213/ab4c99

David, T. J., Hillenbrand, L. A., Petigura, E. A., et al. 2016, Nature, 534, 658, doi: 10.1038/nature18293

David, T. J., Crossfield, I. J. M., Benneke, B., et al. 2018, AJ, 155, 222, doi: 10.3847/1538-3881/aabde8

Díaz, R. F., Rey, J., Demangeon, O., et al. 2016, A&A, 591, A146, doi: 10.1051/0004-6361/201628331

Douglas, S. T., Agüeros, M. A., Covey, K. R., et al. 2016, ApJ, 822, 47, doi: 10.3847/0004-637X/822/1/47

Douglas, S. T., Curtis, J. L., Agüeros, M. A., et al. 2019, ApJ, 879, 100, doi: 10.3847/1538-4357/ab2468

Doyle, A. P., Davies, G. R., Smalley, B., Chaplin, W. J., & Elsworth, Y. 2014, MNRAS, 444, 3592, doi: 10.1093/mnras/stu1692

Duncan, M. J., Levison, H. F., & Lee, M. H. 1998, AJ, 116, 2067, doi: 10.1086/300541

Eggen, O. J. 1965, The Observatory, 85, 104

Ehrenreich, D., Bourrier, V., Wheatley, P. J., et al. 2015, Nature, 522, 459, doi: 10.1038/nature14501

Evans, D. W., Riello, M., De Angeli, F., et al. 2018, A&A, 616, A4, doi: 10.1051/0004-6361/201832756

Falcón-Barroso, J., Sánchez-Blázquez, P., Vazdekis, A., et al. 2011, A&A, 532, A95, doi: 10.1051/0004-6361/201116842

Fang, J., & Margot, J.-L. 2013, ApJ, 767, 115, doi: 10.1088/0004-637X/767/2/115

Főrész, G. 2008, PhD thesis, University of Szeged

Fischer, D. A., Marcy, G. W., & Spronck, J. F. P. 2014, ApJS, 210, 5, doi: 10.1088/0067-0049/210/1/5

Foreman-Mackey, D. 2016, The Journal of Open Source Software, 1

Foreman-Mackey, D., Agol, E., Angus, R., & Ambikasaran, S. 2017, ArXiv. https://arxiv.org/abs/1703.09710

Foreman-Mackey, D., Hogg, D. W., Lang, D., & Goodman, J. 2013, PASP, 125, 306, doi: 10.1086/670067

Fortney, J. J., Ikoma, M., Nettelmann, N., Guillot, T., & Marley, M. S. 2011, ApJ, 729, 32, doi: 10.1088/0004-637X/729/1/32

Fuhrmann, K. 2008, MNRAS, 384, 173, doi: 10.1111/j.1365-2966.2007.12671.x

Fulton, B. J., & Petigura, E. A. 2018, AJ, 156, 264, doi: 10.3847/1538-3881/aae828

Gagné, J., Mamajek, E. E., Malo, L., et al. 2018, ApJ, 856, 23, doi: 10.3847/1538-4357/aaae09

Gaidos, E., Hirano, T., Mann, A. W., et al. 2020, MNRAS, 495, 650, doi: 10.1093/mnras/staa918

Gaidos, E. J. 1998, PASP, 110, 1259, doi: 10.1086/316251

Gaidos, E. J., Henry, G. W., & Henry, S. M. 2000, AJ, 120, 1006, doi: 10.1086/301488

Gao, P., & Zhang, X. 2020, ApJ, 890, 93, doi: 10.3847/1538-4357/ab6a9b

Ginzburg, S., Schlichting, H. E., & Sari, R. 2018, MNRAS, 476, 759, doi: 10.1093/mnras/sty290

Henden, A. A., Templeton, M., Terrell, D., et al. 2016, VizieR Online Data Catalog, II/336

Hinkel, N. R., Timmes, F. X., Young, P. A., Pagano, M. D., & Turnbull, M. C. 2014, AJ, 148, 54, doi: 10.1088/0004-6256/148/3/54

Hirano, T., Suto, Y., Winn, J. N., et al. 2011, ApJ, 742, 69, doi: 10.1088/0004-637X/742/2/69

Høg, E., Fabricius, C., Makarov, V. V., et al. 2000, A&A, 355, L27

Horne, J. H., & Baliunas, S. L. 1986, ApJ, 302, 757, doi: 10.1086/164037

Huang, J., Andrews, S. M., Dullemond, C. P., et al. 2018, ApJL, 869, L42, doi: 10.3847/2041-8213/aaf740

Huber, D., Carter, J. A., Barbieri, M., et al. 2013, Science, 342, 331, doi: 10.1126/science.1242066

Hunter, J. D. 2007, Computing in science & engineering, 9, 90

Jenkins, J. M., Twicken, J. D., McCauliff, S., et al. 2016, in Society of Photo-Optical Instrumentation Engineers (SPIE) Conference Series, Vol. 9913, Proc. SPIE, 99133E, doi: 10.1117/12.2233418

Johnson, M. C., Dai, F., Justesen, A. B., et al. 2018, MNRAS, 481, 596, doi: 10.1093/mnras/sty2238

Jones, J., White, R. J., Boyajian, T., et al. 2015, ApJ, 813, 58, doi: 10.1088/0004-637X/813/1/58

Kaib, N. A., Raymond, S. N., & Duncan, M. 2013, Nature, 493, 381, doi: 10.1038/nature11780

Kane, S. R. 2015, ApJL, 814, L9, doi: 10.1088/2041-8205/814/1/L9

—. 2019, AJ, 158, 72, doi: 10.3847/1538-3881/ab2a09

Kane, S. R., & Blunt, S. 2019, AJ, 158, 209, doi: 10.3847/1538-3881/ab4c3e

King, J. R., & Schuler, S. C. 2005, PASP, 117, 911, doi: 10.1086/432457

King, J. R., Villarreal, A. R., Soderblom, D. R., Gulliver, A. F., & Adelman, S. J. 2003, AJ, 125, 1980, doi: 10.1086/368241

Kipping, D. M. 2013, MNRAS, 435, 2152, doi: 10.1093/mnras/stt1435

—. 2014, MNRAS, 444, 2263, doi: 10.1093/mnras/stu1561

Kipping, D. M., Schmitt, A. R., Huang, X., et al. 2015, ApJ, 813, 14, doi: 10.1088/0004-637X/813/1/14

Kovács, G., Zucker, S., & Mazeh, T. 2002, A&A, 391, 369, doi: 10.1051/0004-6361:20020802

Kraus, A. L., Herczeg, G. J., Rizzuto, A. C., et al. 2017, ApJ, 838, 150, doi: 10.3847/1538-4357/aa62a0

Kreidberg, L. 2015, PASP, 127, 1161, doi: 10.1086/683602

Kurucz, R. 1993, ATLAS9 Stellar Atmosphere Programs and 2 km/s grid. Kurucz CD-ROM No. 13. Cambridge, 13

Li, G., Naoz, S., Valsecchi, F., Johnson, J. A., & Rasio, F. A. 2014, ApJ, 794, 131, doi: 10.1088/0004-637X/794/2/131

Li, J., Tenenbaum, P., Twicken, J. D., et al. 2019, PASP, 131, 024506, doi: 10.1088/1538-3873/aaf44d

Libby-Roberts, J. E., Berta-Thompson, Z. K., Désert, J.-M., et al. 2020, AJ, 159, 57, doi: 10.3847/1538-3881/ab5d36

Lindegren, L., Hernández, J., Bombrun, A., et al. 2018, A&A, 616, A2, doi: 10.1051/0004-6361/201832727

Lopez, E. D., & Fortney, J. J. 2013, ApJ, 776, 2, doi: 10.1088/0004-637X/776/1/2

—. 2014, ApJ, 792, 1, doi: 10.1088/0004-637X/792/1/1

Luck, R. E. 2017, AJ, 153, 21, doi: 10.3847/1538-3881/153/1/21

Madsen, S., Dravins, D., & Lindegren, L. 2002, A&A, 381, 446, doi: 10.1051/0004-6361:20011458

Maíz Apellániz, J., & Weiler, M. 2018, A&A, 619, A180, doi: 10.1051/0004-6361/201834051

Mamajek, E. E., Kenworthy, M. A., Hinz, P. M., & Meyer, M. R. 2010, AJ, 139, 919, doi: 10.1088/0004-6256/139/3/919

Mann, A. W., Feiden, G. A., Gaidos, E., Boyajian, T., & von Braun, K. 2015, ApJ, 804, 64, doi: 10.1088/0004-637X/804/1/64

Mann, A. W., & von Braun, K. 2015, PASP, 127, 102, doi: 10.1086/680012

Mann, A. W., Gaidos, E., Mace, G. N., et al. 2016a, ApJ, 818, 46, doi: 10.3847/0004-637X/818/1/46

Mann, A. W., Newton, E. R., Rizzuto, A. C., et al. 2016b, AJ, 152, 61, doi: 10.3847/0004-6256/152/3/61

Mann, A. W., Gaidos, E., Vanderburg, A., et al. 2017, AJ, 153, 64, doi: 10.1088/1361-6528/aa5276

Mann, A. W., Vanderburg, A., Rizzuto, A. C., et al. 2018, AJ, 155, 4, doi: 10.3847/1538-3881/aa9791

Marsden, S. C., Petit, P., Jeffers, S. V., et al. 2014, MNRAS, 444, 3517, doi: 10.1093/mnras/stu1663

Martín, E. L., Lodieu, N., Pavlenko, Y., & Béjar, V. J. S. 2018, ApJ, 856, 40, doi: 10.3847/1538-4357/aaaeb8

Mason, B. D., Wycoff, G. L., Hartkopf, W. I., Douglass, G. G., & Worley, C. E. 2001a, AJ, 122, 3466, doi: 10.1086/323920

—. 2001b, AJ, 122, 3466, doi: 10.1086/323920

Masuda, K., & Winn, J. N. 2020, AJ, 159, 81, doi: 10.3847/1538-3881/ab65be

McCully, C., Volgenau, N. H., Harbeck, D.-R., et al. 2018, in Society of Photo-Optical Instrumentation Engineers (SPIE) Conference Series, Vol. 10707, Software and Cyberinfrastructure for Astronomy V, 107070K, doi: 10.1117/12.2314340

McQuillan, A., Aigrain, S., & Mazeh, T. 2013, MNRAS, 432, 1203, doi: 10.1093/mnras/stt536

Mermilliod, J.-C., Mermilliod, M., & Hauck, B. 1997, A&AS, 124, 349, doi: 10.1051/aas:1997197

Montet, B. T., Feinstein, A. D., Luger, R., et al. 2020, AJ, 159, 112, doi: 10.3847/1538-3881/ab6d6d

Mortier, A., Sousa, S. G., Adibekyan, V. Z., Brand ão, I. M., & Santos, N. C. 2014, A&A, 572, A95, doi: 10.1051/0004-6361/201424537

Moultaka, J., Ilovaisky, S. A., Prugniel, P., & Soubiran, C. 2004, PASP, 116, 693, doi: 10.1086/422177

Murray-Clay, R. A., Chiang, E. I., & Murray, N. 2009, ApJ, 693, 23, doi: 10.1088/0004-637X/693/1/23

Newton, E. R., Mann, A. W., Tofflemire, B. M., et al. 2019, ApJL, 880, L17, doi: 10.3847/2041-8213/ab2988

Nidever, D. L., Marcy, G. W., Butler, R. P., Fischer, D. A., & Vogt, S. S. 2002, ApJS, 141, 503, doi: 10.1086/340570

Ninan, J. P., Stefansson, G., Mahadevan, S., et al. 2020, ApJ, 894, 97, doi: 10.3847/1538-4357/ab8559

Obermeier, C., Henning, T., Schlieder, J. E., et al. 2016, AJ, 152, 223, doi: 10.3847/1538-3881/152/6/223

Oh, S., Price-Whelan, A. M., Hogg, D. W., Morton, T. D., & Spergel, D. N. 2017, AJ, 153, 257, doi: 10.3847/1538-3881/aa6ffd

Owen, J. E. 2019, Annual Review of Earth and Planetary Sciences, 47, 67, doi: 10.1146/annurev-earth-053018-060246

Owen, J. E., & Jackson, A. P. 2012, ArXiv e-prints. https://arxiv.org/abs/1206.2367

Owen, J. E., & Wu, Y. 2013, ApJ, 775, 105, doi: 10.1088/0004-637X/775/2/105

Parviainen, H., & Aigrain, S. 2015, MNRAS, 453, 3821, doi: 10.1093/mnras/stv1857

Pepe, F., Mayor, M., Galland, F., et al. 2002, A&A, 388, 632, doi: 10.1051/0004-6361:20020433

Perruchot, S., Kohler, D., Bouchy, F., et al. 2008, in Society of Photo-Optical Instrumentation Engineers (SPIE) Conference Series, Vol. 7014, Proc. SPIE, 70140J, doi: 10.1117/12.787379

Proctor, R. A. 1869, Proceedings of the Royal Society of London Series I, 18, 169

Raghavan, D., Farrington, C. D., ten Brummelaar, T. A., et al. 2012, ApJ, 745, 24, doi: 10.1088/0004-637X/745/1/24

Raghavan, D., McAlister, H. A., Henry, T. J., et al. 2010, ApJS, 190, 1, doi: 10.1088/0067-0049/190/1/1

Ramírez, I., Fish, J. R., Lambert, D. L., & Allende Prieto, C. 2012, ApJ, 756, 46, doi: 10.1088/0004-637X/756/1/46

Rasmuson, N. H. 1921, Meddelanden fran Lunds Astronomiska Observatorium Serie II, 26, 3

Rayner, J. T., Cushing, M. C., & Vacca, W. D. 2009, ApJS, 185, 289, doi: 10.1088/0067-0049/185/2/289

Rebull, L. M., Stauffer, J. R., Bouvier, J., et al. 2016, AJ, 152, 113, doi: 10.3847/0004-6256/152/5/113

Ricker, G. R., Winn, J. N., Vanderspek, R., et al. 2014, in Society of Photo-Optical Instrumentation Engineers (SPIE) Conference Series, Vol. 9143, 20, doi: 10.1117/12.2063489

Rizzuto, A. C., Ireland, M. J., & Robertson, J. G. 2011, MNRAS, 416, 3108, doi: 10.1111/j.1365-2966.2011.19256.x

Rizzuto, A. C., Mann, A. W., Vanderburg, A., Kraus, A. L., & Covey, K. R. 2017, AJ, 154, 224, doi: 10.3847/1538-3881/aa9070

Rizzuto, A. C., Vanderburg, A., Mann, A. W., et al. 2018, AJ, 156, 195, doi: 10.3847/1538-3881/aadf37

Schlieder, J. E., Skemer, A. J., Maire, A.-L., et al. 2016, ApJ, 818, 1, doi: 10.3847/0004-637X/818/1/1

Schmitt, A. R., Hartman, J. D., & Kipping, D. M. 2019, arXiv e-prints, arXiv:1910.08034. https://arxiv.org/abs/1910.08034

Schwamb, M. E., Orosz, J. A., Carter, J. A., et al. 2013, ApJ, 768, 127, doi: 10.1088/0004-637X/768/2/127

Sfeir, D. M., Lallement, R., Crifo, F., & Welsh, B. Y. 1999, A&A, 346, 785

Siverd, R. J., Brown, T. M., Barnes, S., et al. 2018, in Society of Photo-Optical Instrumentation Engineers (SPIE) Conference Series, Vol. 10702, Proc. SPIE, 107026C, doi: 10.1117/12.2312800

Skrutskie, M. F., Cutri, R. M., Stiening, R., et al. 2006, AJ, 131, 1163, doi: 10.1086/498708

Smith, J. C., Stumpe, M. C., Van Cleve, J. E., et al. 2012, PASP, 124, 1000, doi: 10.1086/667697

Soderblom, D. R., & Mayor, M. 1993, AJ, 105, 226, doi: 10.1086/116422

Somers, G., & Pinsonneault, M. H. 2015, MNRAS, 449, 4131, doi: 10.1093/mnras/stv630

Sousa, S. G., Santos, N. C., Israelian, G., Mayor, M., & Udry, S. 2011, A&A, 533, A141, doi: 10.1051/0004-6361/201117699

Sousa, S. G., Santos, N. C., Mortier, A., et al. 2015, A&A, 576, A94, doi: 10.1051/0004-6361/201425227

Stassun, K. G., Oelkers, R. J., Pepper, J., et al. 2018, AJ, 156, 102, doi: 10.3847/1538-3881/aad050

Stassun, K. G., Oelkers, R. J., Paegert, M., et al. 2019, AJ, 158, 138, doi: 10.3847/1538-3881/ab3467

Stumpe, M. C., Smith, J. C., Catanzarite, J. H., et al. 2014, PASP, 126, 100, doi: 10.1086/674989

Tabernero, H. M., Montes, D., González Hernández, J. I., & Ammler-von Eiff, M. 2017, A&A, 597, A33, doi: 10.1051/0004-6361/201322526

Thao, P. C., Mann, A. W., Johnson, M. C., et al. 2020, AJ, 159, 32, doi: 10.3847/1538-3881/ab579b

Twicken, J. D., Catanzarite, J. H., Clarke, B. D., et al. 2018, PASP, 130, 064502, doi: 10.1088/1538-3873/aab694

Van Cleve, J. E., Howell, S. B., Smith, J. C., et al. 2016, PASP, 128, 075002, doi: 10.1088/1538-3873/128/965/075002

Van Eylen, V., & Albrecht, S. 2015, ApJ, 808, 126, doi: 10.1088/0004-637X/808/2/126

van Leeuwen, F., Evans, D. W., Grenon, M., et al. 1997, A&A, 323, L61

van Saders, J. L., Ceillier, T., Metcalfe, T. S., et al. 2016, Nature, 529, 181, doi: 10.1038/nature16168

Vanderburg, A., Mann, A. W., Rizzuto, A., et al. 2018, AJ, 156, 46, doi: 10.3847/1538-3881/aac894

Vanderburg, A., Huang, C. X., Rodriguez, J. E., et al. 2019, ApJL, 881, L19, doi: 10.3847/2041-8213/ab322d

Vereshchagin, S. V., Chupina, N. V., & Postnikova, E. S. 2018, Astronomy Reports, 62, 502, doi: 10.1134/S1063772918080085

Vogt, S. S. 1987, PASP, 99, 1214, doi: 10.1086/132107

von Braun, K., Boyajian, T. S., Kane, S. R., et al. 2012, ApJ, 753, 171, doi: 10.1088/0004-637X/753/2/171

Wang, J., Fischer, D. A., Barclay, T., et al. 2013, ApJ, 776, 10, doi: 10.1088/0004-637X/776/1/10

Wang, L., & Dai, F. 2019, ApJ, 873, L1, doi: 10.3847/2041-8213/ab0653

Winn, J. N., Holman, M. J., Henry, G. W., et al. 2007, AJ, 133, 1828, doi: 10.1086/512159

Zhou, G., Rodriguez, J. E., Vanderburg, A., et al. 2018, AJ, 156, 93, doi: 10.3847/1538-3881/aad085

Zhou, G., Winn, J. N., Newton, E. R., et al. 2020, ApJL, 892, L21, doi: 10.3847/2041-8213/ab7d3c

Ziegler, C., Law, N. M., Baranec, C., et al. 2018, AJ, 156, 259, doi: 10.3847/1538-3881/aad80a